Insights into the formation of the Stuart Shelf iron-oxide-copper-gold (uranium) system from magnetotellurics.

The University of Adelaide, 2010

Scott Weber

Supervisor: Kate Selway

Co-Supervisor: Stephan Thiel

Insights into the formation of the Stuart Shelf iron-oxide-copper-gold (uranium) system from magnetotellurics. 3
Author 3
Abstract 3
Introduction 3
Geological Background 6
Methods 11
MT Data 11
Processing 13
Dimensionality analysis 14
Modelling 16
Discussion 20
Conclusion 24
Acknowledgements 25
References 26
Figure Captions 30
Appendix 32
Figures 33

Insights into the formation of the Stuart Shelf iron-oxide-copper-gold (uranium) system from magnetotellurics.

Author

Weber, Scott

Abstract

The Gawler Craton, South Australia, is host to many economic ore resources. Of which, iron oxide copper-gold deposits, such as Olympic Dam, Carrapateena and Wirrda Well, stand out due to the quality and abundance of their ore resources. Understanding the mechanisms of their formation is vital for defining exploration models for future development. 166 stations of magnetotelluric data at periods between10^{1}-10^{4} seconds have been used to produce three, 2D models that provide insight into the electrical conductivity of the sub-surface beneath the Stuart Shelf. Links between corresponding regions of conductivity across profiles are shown by faults. It is suggested here that the faults are the fluid flow pathways for the mineralizing hydrothermal fluids. These fluids have been derived from the mantle and the surface in two phases of fluid flow causing both deposition and destruction of graphite respectively.

Introduction

Iron oxide copper-gold (IOCG) deposits comprise some of the world's richest sources of copper, gold and other resources (Hitzman et al., 1992). However, despite their importance, there is significant uncertainty regarding their formation. There are many models of formation that have been proposed for this style of deposit over the last 35 years. For example, Williams et al (2005) suggested that the major problem in IOCG genesis is whether there is a direct link to the mantle or lower crust via magmas, particularly in respect to very large deposits. Some authors have suggested that the deposits are generated

entirely within the crust, in giant hydrothermal systems that were able to effectively concentrate metals that had previously been dispersed through large masses of rocks (Bastrakov et al., 2007; Skirrow et al., 2007). Recent review papers by Groves et al (2010) and Williams et al (2005) have summarised the characteristics of IOCG deposits. Features found to be common to IOCG deposits include: sensu stricto hydrothermal processes associated with magmatism; large quantities of economic metals, specifically copper and gold; being structurally controlled and commonly associated with breccias; being surrounded by alteration and/or brecciation zones on a larger, regional scale relative to economic mineralization; having a lack of abundant synsulphide quartz veins and alteration; having abundant low Ti iron oxides (magnetite, haematite) or iron silicates (grunerite, Fe actinolite, fayalite); LREE enrichment and low S sulphides, including chalcopyrite-bornite-chalcocite and pyrrhotite and having a close temporal, but not an apparent spatial relationship to causative intrusions (Groves et al., 2010; Williams et al., 2005).

An important type example of the IOCG class of deposits is the Olympic Dam Cu-Au-U deposit (Reeve et al., 1990; Roberts and Hudson, 1983). This deposit, located in South Australia on the Stuart Shelf is breccia-hosted and contains large amounts of iron-containing minerals such as magnetite and hematite, copper sulphide minerals such as chalcopyrite, bornite and chalcocite as well as native gold and uranium in the form of uraninite, pitchblende, conite and brannerite (Oreskes and Einaudi, 1990; Roberts and Hudson, 1983). Apart from Olympic Dam, the Stuart Shelf is host to several IOCG deposits and prospects including Prominent Hill (Belperio et al., 2007), Carrapateena (Fairclough, 2005; Vella and Emerson, 2009) and Wirrda Well (Vella, 1997).

As for IOCG deposits as a class, there is considerable debate regarding the formation of the mineralising system in the Stuart Shelf. Skirrow et al (2007) presented evidence in the form of ε_{Nd} ratios to suggest that the formation of the Olympic Dam IOCG was associated with mantle fluids. Rocks with lower ε_{Nd} ratios have been present in a crustal environment longer, while a higher

ε_{Nd} ratio represents a more recent emplacement in the crust. At Olympic dam it can be seen that the mineralized rocks of the deposit have a higher ε_{Nd} ratio then the unmineralized host rocks and subsequently have had more recent mantle-derived activity (Skirrow et al., 2007). A comparison of ε_{Nd} for various rock types at Olympic Dam and at other deposits in the Stuart Shelf was also conducted. It showed that the other deposits have lower ε_{Nd} ratios associated with the mineralization, indicating that in those deposits the mineralisation was not carried with mantle fluids (Skirrow et al., 2007; Skirrow et al., 2006).
A model for the formation of deposits in the Olympic Dam region was also produced, with mantle-penetrating fluid flow beneath Olympic Dam being the source of the mineralization, while mineralization at the other deposits in the region was caused by remobilisation of the mineralization from the host rock. It is also suggested through oxygen isotope evidence that meteoric fluids concentrated the mineralization at Olympic Dam (Skirrow et al., 2007). The fluid-flow pathways suggested are the Andamooka Fault zone and associated northwest-trending splays (Skirrow et al., 2007).

A model for the formation of the Olympic Dam deposit by Groves et al (2010) adapted from Hart et al., (2004) suggests that the deposit formed from partial melting of metasomatized subcontinental lithospheric mantle (SCLM). This produced basic and ultrabasic melt which was probably alkaline and enriched in volatiles as well as copper and gold. The authors suggest that the melt then ponded at the crust-mantle boundary (Moho) where it produced felsic melts and transferred some of the enriched volatiles and Cu/Au. Felsic plutons formed from the ascending melt followed by the basic/ultrabasic melts that produced mafic/ultramafic intrusions in the same region. Thus the exsolution of the deep volatiles produces giant breccia pipes where the alteration by iron oxides, copper, gold, uranium and other rare earth elements occurs.

Oreskes and Einaudi (1990) suggested that deposits in the Olympic Dam region were likely to have formed in hydrothermal systems that contained large quantities of surface-derived water shown by fluid inclusions and oxygen stable isotope data. Further conclusions by Bastrakov et al (2007) suggest support for a two-stage hydrothermal model of formation, consisting of

haematitic alteration overprinting magnetite-bearing assemblages. Measured ratios of Br/Cl indicate the sources of the fluids to be brines rather than magmas, while oxygen and hydrogen values are also not consistent with primary magmatic water source. It is suggested that they could be of metamorphic origin, however they may also be products of local ^{18}O-enriched magmatic waters related to the GRV and Hiltaba Suite, re-equilibration of primary magmatic waters with the host-rock sequences or mixing of the primary magmatic fluid with fluids of a non-magmatic origin (Bastrakov et al., 2007).

IOCG deposits in the Stuart Shelf region are buried beneath several hundred metres of late Proterozoic to Cambrian sediments and geophysics is therefore a vital tool to determine their structure and distinguish between the different models of formation that have been proposed. Magnetotellurics (MT) is a passive electromagnetic geophysical method that is a useful tool to image the electrical resistivity of the Earth. It is effective at showing lithospheric structure which has been proven in other regions of Australia (Selway et al., 2006; Selway et al., 2009b) and around the world (Menezes and Travassos, 2010; Wannamaker and Doerner, 2002; Wannamaker et al., 1997). For example, it has been effective in the past at highlighting fossil fluid pathways (Heinson et al., 2006) as well as the location and dip of a relict Proterozoic subduction zone (Selway et al., 2009a). This paper describes a regional-scale, 3D MT survey in the Stuart Shelf region that was carried out with the aim of constraining proposed models for the formation of the IOCG system.

Geological Background

The Stuart Shelf region sits on the eastern margin of the Archean to Proterozoic Gawler Craton. The Gawler Craton has been described in depth by Hand et al (2007) and the main lithologies and events believed to be important in shaping the Stuart Shelf regions are summarized within. Tectonic activity in the Gawler Craton is concentrated in two separate phases, the first

in the late Archean between 2550 and 2500 Ma and the second in the late Paleoproterozoic and early Mesoproterozoic between 1900 and 1450 Ma (Hand et al., 2007).

Archean rocks are represented by the highly deformed interlayered paragneisses and orthogneisses of the Sleaford Complex and the Mulgathing Complex that outcrop in the southwest and centre-west of the craton respectively (Fraser et al., 2007). The Archean core is surrounded by a series of extensional, collisional, basin-forming and magmatic events formed as belts in the Proterozoic between 1900 and 1450 Ma (Hand et al., 2007), however isotopic evidence exists for Archean lower crust in the eastern Gawler Craton (Creaser, 1995; Stewart and Foden, 2003). The Hutchison Group metasediments is the oldest outcropping lithological unit in the Olympic Dam region, which has been interpreted to have a maximum deposition age of 2000 Ma (Fanning et al., 1988). This sedimentary sequence includes the Middleback Subgroup, an economically important unit which contains iron-ore hosting iron formations. Subsequently the Hutchison Group was intruded by the ca. 1850 Ma Donington Suite, which has an ε_{Nd} signature that has been interpreted to represent a mantle source contaminated by Archean lower crust (Mortimer et al., 1988).

The eastern margin was then host to post-Donington suite rifting, indicated by the eruption of bimodal Myola Volcanics at 1791Ma. A continuing depositional period ca. 1770-1740Ma started with the formation of the Price Metasediments ca. 1767 ± 17 Ma, (Oliver and Fanning, 1997) , the Wallaroo Group ca. 1760–1740 Ma (Cowley et al., 2003), the Moonabie Formation ca. 1756 ± 8 Ma (Jagodzinski, 2005)) and the McGregor Volcanics ca. 1740 Ma (Fanning et al., 1988), which have an ε_{Nd} signature that indicates crustal contamination of a mantle melt, shown by (Turner et al., 1993). This was followed by an extensive period of igneous events. The Tunkillia Suite, formed ca. 1690-1670, is an I-type intrusion and occurs as discrete plutons in the central Gawler craton (Ferris and Schwarz, 2004; Payne et al., 2010)**.** Nuyts Volcanics erupted in the south-western Gawler craton, ca. 1630Ma (Cooper et al., 1985; Rankin et al., 1990) and were subsequently intruded by the St.

Peter Suite ca. 1620-1610Ma (Flint et al., 1990), which has been interpreted to have formed in a subduction-related environment (Swain et al., 2005).

A major co-magmatic event occurred ca. 1595-1575Ma: the Gawler Range Volcanics (GRV) - Hiltaba Suite event, which is associated with a major tectonothermal and metallogenic period (Budd et al., 2001; Daly et al., 1998; Hand et al., 2007; Skirrow et al., 2002). The Hiltaba Suite is linked to gold mineralization in the central Gawler Craton (Ferris and Schwarz, 2004) and is also temporally and spatially associated with regional-scale iron and sodium-calcium alteration and subsequently the Cu-Au-U mineralization (Skirrow et al., 2002). The GRV located across the Gawler craton is felsic in nature and consists of an upper and lower sequence that were deposited over a short period of time shown by their indistinguishable ID-TIMS U-Pb zircon age dates (Blissett et al., 1993; Fanning et al., 1988). The Olympic Dam region is covered by several hundred metres of Stuart Shelf sediments. These sediments form part of a package of Neoproterozoic to Cambrian rift sediments that extend several hundred kilometres to the east and at least several hundred kilometres to the south, collectively called the Adelaide Geosyncline (Priess, 1987).

The first major tectonic event to affect the Gawler Craton was the 2480-2420 Ma Sleafordian Orogeny (Daly et al., 1998). The compressional 1730-1690 Ma Kimban Orogen appears to have affected the entire Gawler Craton (Payne et al., 2006) and the dominant structural architecture in the eastern Gawler Craton was formed during this event (Hand et al., 2007). Deformation occurred in association with the Hiltaba Suite magmatism in the period ca. 1595–1575 Ma, which coincides with the Olarian orogeny in the adjacent Curnamona Province which exhibits northwest-southeast compression. Due to the lack of extensional evidence usually associated with magmatism, it has been suggested that the deformational situation was that of shortening/compression (Direen and Lyons, 2007; Hand et al., 2007). Furthermore, from the co-magmatic event, it is suggested deformation was driven by a component of northwest-southeast–directed shortening (Hand et

al., 2007). The shortening was most likely absorbed by the shear zones that bound the Archean core. This reactivation of both north-south and east-west trending faults is likely to have controlled the fluid flow pathways in the region and subsequently have been interpreted to have played a role in mineralization (Direen and Lyons, 2007; Hand et al., 2007; Reeve et al., 1990; Skirrow et al., 2002).

Olympic Dam (Roberts and Hudson, 1983) is hosted within a haematite-dominated breccia complex hosted by the Burgoyne batholith, part of the Hiltaba Suite (Blissett et al., 1993; Oreskes and Einaudi, 1990; Reeve et al., 1990). It is a structurally controlled, hydrothermal deposit, which formed at a depth of less then 5 km not long after the formation of the host (Creaser, 1995). Major sulphides in the ore are pyrite (FeS_2), chalcopyrite ($CuFeS_2$), bornite (Cu_5FeS_4), and chalcocite (Cu_2S), while other minor sulphides, native metals, selenides and tellurides are also present (Oreskes and Einaudi, 1992; Reeve et al., 1990). The Roxby Downs Granite (Creaser, 1995) is the host rock for the deposit, which has approximately 60% alkali feldspar, 20% quartz and 20% plagioclase, with accessory biotite, amphibole, magmatic magnetite, apatite and zircon. This granite is found several kilometres away from the deposit unaltered. The deposit is surrounded by hematite, chlorite and serecite altered granite as well as brecciated granite that has many veins and has been hydrothermally altered. While this breccia contains under 35% hematite and clasts of the altered granite, closer to the barren core, hematite breccias become dominant with 35 to 90% hematite (Oreskes and Einaudi, 1990). This breccia contains clasts of granite, hematite from early phases, siderite, fluorite and barite clasts and is very matrix supported. In the centre of the deposit is a barren hematite-quartz breccia core which has a composition of hematite and silica. Dykes are present throughout the deposit and are mafic and ultramafic in composition. These appear to have been injected into the hot unconsolidated material, as they can appear as either distinct units or clasts within the volcanic breccias. These dykes have been altered by both sericite and chlorite or hematite and are rarely mineralised themselves; however they are associated with areas of high grade mineralization.

Volcanics are also present in the deposit as volcaniclastic conglomerates and breccias. These volcanics contain no or very little mineralization and contain no granite components, although the breccia does contain hematite altered phases (Haynes et al., 1995; Hitzman et al., 1992; Oreskes and Einaudi, 1992; Reeve et al., 1990; Roberts and Hudson, 1983).

Two smaller prospects on the Stuart Shelf are Wirrda Well and Carrapateena. Wirrda Well is a granite hosted breccia deposit that has undergone hematite, sericite and chlorite alteration. Hematite and magnetite are associated with mineralization as is chlorite alteration. Mineralization occurs as copper, gold and uranium in the highly altered and veined rocks (Vella, 1997). The Carrapateena deposit is hosted by the Carrapateena Breccia Complex, part of the Donington suite. The host member is a variably foliated and/or sheared gneissic quartz granite and quartz diorite (Vella and Emerson, 2009). The alteration is haematite, sericite and chlorite which hosts to the copper, gold and rare earth element mineralization (Vella and Emerson, 2009). Magnetic data show NE-striking faults superimposed on the overall NW-striking structural fabric, with structures suggested to have localised fluid and magmatic flow during mineralization (Fairclough, 2005).

In the past other forms of geophysical analysis have been conducted on the Stuart Shelf ore systems, including magnetotellurics, seismic reflection and potential field analysis. A magnetotelluric survey conducted by Heinson et al (2006) in a transect from the southwest to northeast centred on Olympic Dam revealed resistive lower crust in the south-west of the model, conductive lower crust in the north-east of the model that extends to a depth of 5km beneath the resistive Burgoyne batholith and resistive middle crust to the north-east of Olympic Dam. The authors suggested that the low resistivity region beneath Olympic Dam may be due to an Au–CO_2-rare earth element–rich fluid pathway and that the upward movement of CO_2 bearing volatiles would have precipitated conductive graphite along grain boundaries. Alternatively, the source of the volatiles may be from mantle degassing or retrograde metamorphism of the lower crust (Heinson et al., 2006).

Seismic reflection data have been used by Drummond et al (2006) to image the region beneath Olympic Dam. They showed that there is an area of weak reflectivity beneath the Burgoyne batholith and the authors proposed this to be the source-region for the granite. The seismic data were interpreted to suggest that the most likely explanation for the elevated lower crustal temperatures that produced the Burgoyne batholith was radiogenic heating (Drummond et al., 2006). A potential field study was undertaken by Direen and Lyons (2007) to integrate regional potential field data with detailed geological observations of the tectonostratigraphic setting of the mineral system. The authors interpreted that the data suggest that the system was compressional during the time of formation and not extensional as suggested by many models and that the association with volcanic rocks is a spatial relationship and not a genetic one (Direen and Lyons, 2007).

Methods

MT Data

Magnetotellurics is a passive (uses naturally induced currents) electromagnetic geophysical technique that can image the electrical resistivity of the Earth to depths up to 600km. The magnetotelluric method is described in depth in Simpson and Bahr (2005). An overview of fundamental features is described here. Electrical resistivity is calculated by measuring the changes in the external magnetic field (Bx, By) and subsequently the induced electrical response of the Earth in the form of the resulting vector electric field (Ex, Ey) and the variational vertical magnetic field (Bz) at the Earth's surface (Swift, 1971; Vozoff, 1972). Electromagnetic (EM) waves travel diffusely, that is to say they attenuate over a distance as they travel through the Earth. As such, different frequencies or periods will provide different depth of imaging. This is based on the instrument's recording ability: with shorter periods you will produce imaging closer to the surface and longer periods (e.g. > 100s) imaging will occur at greater depths, including into the mantle. The skin depth

d, (maximum depth of resolution for a given period) in a homogenous Earth is defined by;

$$d(T) \approx 500\sqrt{T\rho} \quad (1),$$

where T is period and ρ is the resistivity. The magnetic data are then used by themselves to produce induction arrows which are vectors indicating the lateral direction of the electric current in the Earth at certain periods. Induction arrows are defined by complex ratios in the equation;

$$H_z(\omega) = (T_x(\omega)T_y(\omega))\left(\frac{B_x/\mu_0}{B_y/\mu_0}\right) (2),$$

where H is magnetic intensity[3] [in A m^{-1}], ω is angular frequency [s^{-1}], μ_0 is magnetic permeability of free space [H m^{-1}], T_x, T_y are components of induction arrows, $\mathrm{B}_x, \mathrm{B}_y$ are components of the magnetic field.

Real induction arrows in the Parkinson convention point towards the conductive unit. The orthogonal components of the horizontal electric and magnetic field are related through the impedance tensor ($\underline{\underline{Z}}$) composed of both real and imaginary parts. The relationship is described through the equations;

$$\begin{pmatrix} E_x \\ E_y \end{pmatrix} = \begin{pmatrix} Z_{xx} & Z_{xy} \\ Z_{yx} & Z_{yy} \end{pmatrix} \begin{pmatrix} B_x/\mu_0 \\ B_y/\mu_0 \end{pmatrix} \text{ or } E = \underline{\underline{Z}}B/\mu_0 \quad (3);$$

where E is the electric field [Vm^{-1}], E_x, E_y are components of E, $\underline{\underline{Z}}$ is the impedance tensor [V A^{-1}] and its components. Magnetic and electric data can be processed to produce apparent resistivity (ρ_a) and impedance phase (ϕ) information which is used in the dimensionality analysis of the subsurface and to work out the geo-electric strike direction. The apparent resistivity is defined as the average resistivity for an equivalent uniform half-space, defined by the equation;

$$\rho_{a,ij(\omega)} = \frac{1}{\mu_0 \omega} \left| Z_{ij}(\omega) \right|^2 \quad (4).$$

The impedance phase is defined by;

$$\phi_{ij} = \tan^{-1}\left(\frac{\mathrm{Im}\{Z_{ij}\}}{\mathrm{Re}\{Z_{ij}\}} \right) \quad (5).$$

The electric and magnetic fields are inverted to produce the model of the electrical resistivity of the Earth with depth. Transverse Electric (TE) and Transverse Magnetic (TM) are two independent modes that are derived from the transfer function for a two dimensional Earth where induced electric and magnetic fields are perpendicular to inducing fields. TM describes the current flowing perpendicular to the strike for the components E_y, E_z, B_x while TE describes the current flow parallel to the strike for the components B_y, B_z, E_x for a strike in the x-direction (Simpson and Bahr, 2005; Swift, 1971; Vozoff, 1972).

In this survey 166 Stations were used as a regional grid across the Stuart Shelf, shown in Figure 1. Field work was carried out in 2004, 2007, 2008 and 2009 and data were recorded for at least two days. The instruments used to collect the long period data collected 5 components of information, the 3 components of the magnetic field and two horizontal components of the electric field. This was made up of a Bartington fluxgate magnetometer to collect the magnetic field data and pairs of copper/copper sulphate porous pots for the electric field.

Processing

Two processing codes were used to process the time series data. The codes were Robust Remote Reference Magnetotellurics (RRRMT) (Chave and

Thomson, 1989) and the Bounded Influence Remote Reference Processing (BIRRP) (Chave and Thomson, 2004). Remote referencing was carried out on all the stations using magnetic fields recorded simultaneously to reduce the effect of noise on the signal. The data collected in 2008 were processed this year using the RRRMT code as they had not been processed previously. The 2008 dataset consisted of 7 stations, each of which was individually processed and then analysed for remote referencing. Since the data were not recorded using accurate timing devices, remote referencing required manually matching up magnetic field data from a period of time with data collected from a simultaneously recording station using matlab. Apparent resistivity and phase curves from a station from each year are shown in Figure 2. Stations from the 2009 dataset that appeared to be of poor quality were also reprocessed but the results did not improve, indicating poor data quality for the 15 stations. Processed data provide apparent resistivity and phase data which can be used for interpretation of the data quality and after analysis of all 166 stations it could be seen that there was good quality, consistent (based on proximity) data in a period range of 10s to 4000s. Inductions arrows were also produced which show consistent regional trends. Induction arrow data at periods 100 seconds, 500 seconds, 1000 seconds and 2000 seconds are shown in Figure 3.

Dimensionality analysis

Dimensionality analysis is important to determine the number of directions in which the Earth's resistivity changes. This reflects the models that must be used on the data to provide an accurate representation. For example, a two dimensional model is unable to produce accurate results when the data used are three dimensional in nature. To determine the dimensionality of a dataset the phase tensor (Caldwell et al., 2004) was used in analysis. The phase tensor is characterized by the minimum and maximum phase values, the difference in which produces the ellipticity. The 2D phase tensor can be represented graphically in the form of an ellipsoid. The ellipticity value is the measure of the circularity of the ellipse. At values of less then 0.1 the data are

suggested to be one dimensional, when greater then 0.1, it can be either two or three dimensional, when 1D, the graphical representation of the phase tensor is a symmetrical circle, while when the data or 2D or 3D, it is an ellipse that has an axis aligned perpendicular and parallel to geo-electric strike. The angle of skew is also a parameter of the phase tensor; it is a measure of the tensor's asymmetry. Skew values of less than 5 degrees suggest that the data are one dimensional or two dimensional. The alpha parameter of the phase tensor is the angle of the tensor's dependence on the coordinate system. The orientation of the major axis is alpha - skew and will be parallel to the geo-electric strike (Caldwell et al., 2004). Figure 4 shows how the graphical representation of the phase tensor is created.

Phase tensors were produced for the data collected in 2008 and were analysed together with pre-existing phase tensors for the remaining stations to ascertain the dimensionality of each station at different periods. Due to the large spatial extent of this dataset, it is expected that different trends will be evident in different areas. It was found that the majority of the stations contained period ranges showing both two and three dimensional characteristics with a large proportion of the stations being three dimensional for all periods. It was also found that data at periods greater than 100s and less than 1000s on average were two dimensional, however this also changed with station location due to such a large area being studied. In the central section of the area, it was found that most two dimensional sections had geo-electric strikes of approximately 20 degrees. Areas in the north have geo-electric strikes of 10 degrees and areas in the south a geo-eclectic strike of 40 degrees, however the majority of the two dimensional data have strikes of 20 degrees. The data that were three dimensional have strikes that are period dependent, skews that are outside of ± 5 and ellipticity greater than 0.1. In the cases where ellipticity was below 0.1, with a low skew, the data were said to be one dimensional. The phase tensor analysis, the station locations and assessment of the data quality are attached as appendix 1. Phase tensor ellipses at a period of 128 seconds are shown in Figure 5.

Modelling

Modelling was carried out in both 2D and 3D on a regional scale. The dimensionality analysis constrained what data could be used in these models, as 3D data must not be included in a 2D inversion. 2D inversions must be carried out along profiles that are perpendicular to the geo-electric strike and three profiles were chosen to maximise the number of 2D stations displaying a common strike direction that could be included in the inversion. From the dimensionality analysis, it was known which geo-electric strike best represented the 2D data for each station period. These station groupings were mapped based on their geo-electric strikes and a profile was created that was perpendicular to the geo-electric strike and maximised the available stations. The three 2D models represent geo-electric strikes of 10, 20 and 40 degrees. For data collection, the data are collected with axes orientated north-south and east-west, however this could not be used for modelling purposes. Therefore the station data were rotated individually for each separate model such that the horizontal electric and magnetic fields were orientated parallel and perpendicular to the geo-electric strike.

The Non-Linear Conjugate Gradients algorithm (Rodi and Mackie, 2001) in the WinGlink package was used as the modelling program and the parameters that were altered were tau and the apparent resistivity error floor. Tau represents the offset between smoothness and data fit of the model, with higher tau values representing models that are smoother at the expense of data fit. The final tau value was set to 1 or 3 depending on the profiles' initial modelling. This value was chosen when the models were initially run, starting with the high value of 1000 for tau, decreasing to 300, 100, 30, 10, 3, 1, 0.3 and finally 0.1. This process gradually introduces more structure into the model (Rodi and Mackie, 2001). The value chosen represented the best structure to smoothness ratio, and was chosen from plotting the root mean squared error values (rms), then locating the point where the rms ceased to decrease with decreasing smoothness. The relationship between rms and tau for the 10 degree model is shown in Figure 6. Static shift is a period-independent galvanic distortion that can offset the values of apparent

resistivity but does not affect phase. To correct for any possible static shift errors, inversions were begun with an apparent resistivity error floor of 100%, which was then gradually decreased, using the chosen tau value, to 50%, 30%, 20% and finally 10% to provide maximum representation. The 20, and 40 degree models were set up and run from a starting half space of 100 Ohm metres while the 10 degree model used 500 Ohm metres. Each model underwent multiple iterations with different parameters. The model features were tested for their robustness, while calculations were undertaken to check resolution at depth and breath of the models.

The 20 Degree model spans 85km from the northwest to the southeast crossing the Carrapateena deposit. It incorporates 18 stations of good quality data that represent a geo-electric strike of 20 degrees. The model's skin depth is calculated based on the skin depth equation $_{(1)}$. In this case, the resistivity used was 100 Ohm metres and the longest period was 3000 seconds which calculated to ≈273km. This represents the maximum depth at which the frequencies used have resolution, however as a rule of thumb the model can only be interpreted to a depth no larger than the lateral extent of the profile. The stations are well spaced across the eastern side of the profile situated over the Carrapateena deposit, however the spacing is poor to the west. The stations to the west are grouped closely in two pairs of two. This model can be divided into 6 distinct areas of resistivity, A through F and these labels correspond to Figure 7. Labelled A is a region of resistivity of 1-600 ohm metres in the mid to upper crust, this corresponds to the surface area of the Gawler Range Volcanics (GRV). Labelled C is a region of 500-8000 ohm metres extending from the mantle to the lower crust. Labelled B is a region of 500-8000 ohm meters to the rast of section A in the upper crust, which corresponds to the surface feature of the Donington suite. Labelled F is a region of 1-600 ohm metres in the upper crust that corresponds to the surface location of the Donington suite and includes a multitude of small to medium sized north-south trending faults. This area also hosts the Carrapateena deposit just to the north. Beneath F, labelled E is a region of 600 – 8000 ohm metres in the mid crust. This unit is located next to a large northwest trending fault. Labelled D, located to the west and beneath area E, is an area of

resistivity between 10-500 ohm metres. This region also appears to be associated with the large northwest trending fault.

The 10 degree model spans 65km along an angle 100°E of north, crossing the region between the Carrapateena and Olympic dam deposits. It incorporates 10 stations of good quality data that represent a geo-electric strike of 10 degrees. The models skin depth is ≈ 273km as per the 20 degree model. The stations are also well spaced across three quarters of the model with an outlier to the east. The 10 degree model has 4 regions of resistivity, labelled G through J shown on Figure 8. Labelled H is a region of resistivity between 1-600 ohm metres which is associated with surface features of the Donington Suite and the Gawler Range volcanics. This region covers the extent of the profile for the mid to upper crust and includes many small to large faults, two of which can be traced to intersection with the 20 degree model. Labelled G is a region of resistivity of 500-8000 ohm metres in the upper mantle to mid crust, which has a similar resemblance to the feature E in Figure 7 and to its west is the same northwest trending fault. Labelled I is a resistivity of 10-500 ohm metres extending from the mantle to the upper crust similar to that of D in Figure 7. Labelled J is a region of resistivity of 1-100 ohm metres which corresponds to surface faults that are north-south in nature and intersect the 20 degree model.

The 40 degree model has a profile extent of 70km from the northwest to the southeast and is located below the Carrapateena deposit. It incorporates 10 stations of good quality data that represent a geo-electric strike of 40 degrees. The model's skin depth is ≈273km as per the other models. The stations are well spaced over the entire profile providing a good image of the subsurface. Four areas of resistivity are labelled K through N, these labels correspond to Figure 9. Labelled L is a region of resistivity from 1-500 ohm metres, in the upper crust across the profile. L corresponds to the surface features of the GRV and the Moonabie volcanics and consists of a few smaller faults and two larger faults running north-south that extend up to the 20 degree model. Labelled K, a region of 600-8000 ohm metres in the lower to mid crust, appears to be faulted on its west side by a northeast trending fault. Labelled

M is a region of resistivity of 50-700 ohm metres, which extends from the upper mantle. There are two larger north-south faults that intersect the 20 degree model. Labelled N is a region of resistivity that is from 500-8000 ohm metres, which corresponds to the surface features of the Moonabie volcanics and has the Torrens hinge zone to the east extending from the upper mantle into the mid crust.

3D forward modelling was undertaken to analyse the responses of the entire dataset. 3D forward models were run to identify the different electrical structures and test the data. The forward model was set up in winglink using a 3D mesh containing features of different resistivities. The synthetic data produced by the 3D forward model were compared with the measured station data to test the validity of the input resistivity structure.

A 3D model of sedimentary basins was set up, using depth to basement maps of the different sedimentary basins from the Proterozoic and Phanerozoic and an overall basin 3D model was produced (Figure 10). This was set up to show the impacts of the sedimentary basins on the data. This model showed that the response for the sedimentary basins with a set resistivity of 10 ohm metres in an 400 km vicinity, This provided induction arrows which point mainly towards the east (Figure 11).

A second 3D model was set up that was an extrapolation of the 2D model highlighting the conductive and resistive zones produced (Figure 10). This model is based on a curved conductive region extending from about 15km depth across the stations and surrounding area. This model has been modified multiple times to attempt to replicate the induction arrows processed, in an attempt to represent one of the possible causes for the southeast to east to northeast trending arrows. The model shown however best represents the 2D model's data. The forward model's results show induction arrows that point mainly to the east (Figure 11).

Discussion

The region is shown to contain enhanced conductivity throughout the crust and mantle. There are three completed 2D models for the region which show detailed subsurface resistivity. Of the three models, the most detailed is the 20 degree model which transects the Carrapateena deposit. Common features are observed across the three models (Figure 7, 8 and 9) and in most cases can be linked by faults. A shallow conductor exists for all three models labelled A, F, L and H, which is likely to be the product of downward smoothing on shallow conductive sediments. Feature A however extends to greater depths than the other shallow conductors. This is likely due to the poor constraint on that part of the model. This area also corresponds to the GRV, which could also be conductive, possibly due to hydrated minerals; this process is described later and could contribute to the increased low resistivity thickness. However the GRV is a maximum of 1.5 kilometres thick (Hand et al., 2007), therefore there would still be downward smoothing on the GRV and the sediments in the area. The idea that the GRV is conductive is also supported by observing that two parts of H corresponding to the GRV also show deeper conductivity. A resistive upper crust, labelled B, could be associated with the Hiltaba Suite, however it is offset slightly to the south. A resistive lower crust and upper mantle is also a common feature labelled C and N. These high resistivities are expected from dry, crystalline rock that contains no conductive phase. This area corresponds to the surface GRV and it is expected that the underlying lithologies in this region would be Hiltaba Suite, Donington Suite, Hutchison Group and Archean crust (Hand et al., 2007). All of these units would be expected to have the observed resistivities. D, I, J and M are conductive regions extending from the upper mantle to the lower crust with some dipping lower resistivity features extending to the surface. This area has the same lithologies as the previously described high resistivity, therefore there is no reason lithologically for increased conductivity.

A phase causing enhanced conductivity and subsequently low resistivity region in the Earth must exist in the region of D, I, J and M; therefore it is important to address what could cause this. There are many options for the

cause of the low resistivity including graphite (Glover, 1996), interconnected free fluids, sulphides, melt and hydrated minerals (Nover, 2005). Some of these can be discounted due to other known information about the area and the effects they have on it. Melt is the first to be discounted for this system, as there is an absence of evidence for the existence of partial melt; for example it is not shown in the seismic reflection data (Drummond et al., 2006; Hermance, 1979; Nover, 2005). Sulphides in large quantities would be able to provide the increased conductivity, however they would also produce a large gravity anomaly (Jones et al., 2005; Nover, 2005), which when looking at gravity survey data is not seen in the region to the extent needed. Interconnected free fluids would be able to provided the increased conductivity, however only to shallow depths, because meteoric fluids are unable to cross the brittle-ductile boundary and fluids in the ductile crust are usually removed over time, therefore they do not explain the extent of the resistivity (Wannamaker and Doerner, 2002). Hydrated minerals occur due to the hydrous alteration of minerals. This increases their hydrogen content and subsequently increases their ability to conduct. This indicates the presence of a previous hydrous fluid however does not require the interconnection of porous fluid saturated rocks, as the interconnected free fluid concept does (Nover, 2005). However, hydrated minerals are unlikely as the increased conductivity extends to the surface. This is because it is improbable that the effects of diffusion would be apparent at low temperatures, meaning we could expect diffusion in the upper mantle and the lower crust however not in the upper crust (K. Selway, pers. Comm., 2010)

The main geological difference between the less resistive and more resistive region is the extensive faulting as show in Figure 1. Therefore it is possible that the increased conductivity in this zone is related to fluid flow along shear zones. Graphite (Glover, 1996) would be able to provide this low resistivity, and would explain the resistivity at the depths; however graphite forms in a reducing environment and the Olympic Dam deposit, as well as Carrapateena show signs of an oxidised environment (Roberts and Hudson, 1983; Vella and Emerson, 2009). The lack of reduced minerals at the deposits such as ilmenite support this, as ilmenite is produced due to the removal of titanium

from magnetite with deposition of carbon (graphite) on nearby mineral surfaces which is sourced from fluid CO_2 (Glover, 1996). Carbon derived from mantle degassing would be an option for source of the carbon beneath the deposit based on the ε_{Nd} ratios suggested by Skirrow et al., (2007).

One suggestion is that there were two phases of fluid-flow, the first producing reduced minerals such as graphite and the second fluid-flow phase producing an oxidised environment closer to the surface. E, G and K show higher resistivity in the upper to mid-crustal zones. This area could have been absent of fluid flow, however this area is also subject to a large amount of faulting. These faults however are NS-trending while the faults which are associated with low resistivity are NW-trending. The first phase of fluid-flow containing early mineralization is believed to have travelled along the NW-trending faults (Hayward, N., pers. comm., 2010), while the second meteoric fluid-flow phase could have travelled along the NS-trending faults. The features E, G and K exhibit higher resistivities and only extend from the upper to mid crust (downward smoothing and poor resolution due to a lack of stations is assumed for feature G). The mid crust is a probable approximation for the depth of the brittle-ductile transition and is the maximum depth to which these surface-derived fluids would have likely reached. Features E, G and K are associated with the NS-trending faults. It is suggested that these meteoric oxidising fluids would have destroyed the graphite, producing carbon dioxide and increasing the resistivity of the area. It is therefore possible that the conductive region images the zone of graphite deposition during initial hydrothermal fluid flow along NW-trending faults and this more resistive region images the zone of later oxidising fluid flow that concentrated the mineralising species, oxidising magnetite to hematite and destroying the conductive graphite.

One other 2D model exists for the region proposed by Heinson et al (2006). This model transects the Olympic dam deposit, where there is a resistive middle crust located to the east of a conductive zone that extends from the mantle into the crust, similar to that of the 20 Degree model produced near Carrapateena. This area is also faulted extensively and a similar theory

explaining the resistivities could be applied to this model involving two phases of fluid-flow.

The 3D forward models tests were run to understand the dominant feature that was observed in the induction arrows. There were two theories to induction arrow response; the first was that they were responding to the sedimentary basins in the region. The Gawler Craton is overlain by shallow sedimentary cover; there are also deep basins in the area, the Adelaide Geosyncline to the east and the Cooper/Eromanga Basins in the northeast (Hand et al., 2007). The test was run to see whether the basins alone could be producing the observed induction arrow response. The results show that the sedimentary basins could not alone produce the observed induction arrow response. The second model was for a conductor that curves from the SW > SE > E > NE > NW that extended from the upper mantle to lower crust. This test was run to see if the upper-mantle to mid-crust conductor observed in the models labelled C, D and M and the corresponding conductor in Heinson et al (2006) are connected and are the dominant features producing the response shown by the induction arrows. The results show that this conductor alone does not explain the induction arrows. The results from the 3D forward models show that both models reproduced some of the main data features, however not all of them. The sedimentary basin model did a good job at reproducing the induction arrows that point to the east and then swing around to the northeast. From this, we can assume that sedimentary basins are an important regional-scale conductive feature. Meanwhile the curved conductor mainly produces eastward-trending arrows. A possible combination of the sedimentary basins and features observed in my models would reproduce the induction arrows observed. A 3D inversion would be useful to define this more accurately.

The model proposed by Groves et al (2010) as described previously, suggests a lithospheric-scale system which would derive a deep source of fluids. The fluids would involve a mantle source, indicating the existence of mantle penetrating features. The model involves a metasomatised SCLM,

which would have been produced from an earlier geological event. The initial fluids for this model would likely have been sourced for this metasomatized SCLM and would have contained a large amount of carbon as well as Cu/Au. The secondary concentrating fluids could have been surface-derived fluids that have had interactions with the crustal melts that were associated with the melting and intrusion from the mantle (e.g. fluids associated with the Hiltaba suite magmatism).

Similarly the model proposed by Skirrow et al (2007) for the Olympic Dam system suggests the involvement of mantle-derived hydrothermal fluids running along the NW-trending fault system, with the later-involved surface-derived fluids concentrating the mineralization. The MT models produced here show conductors along the NW-trending fault system further to the south, which do extend to depths into the mantle. At the Carrapateena deposit this conductivity area corresponds to the surface to the west of the deposit, which could indicate the need of a secondary process that remobilized the mineralization to the deposit, perhaps surface-derived fluids. The ideas proposed here do not contradict the models proposed by Groves et al (2010) and Skirrow et al (2007). They also do not contradict the theories proposed by Oreskes and Einaudi (1990) and Bastrakov et al (2007), which include a dual-phase hydrothermal alteration system.

Conclusion

This project has aimed to provide an insight into the formation of IOCG deposits in the Stuart Shelf region, South Australia by constraining proposed models. This area is covered by a think layer of sediments, which makes geophysics a vital tool in determining their structure and the structure of the surrounding region. Magnetotelluric data were collected over a period of 4 years, making up a survey of 166 stations that were able to be used in a regional grid across the Stuart Shelf. Three two dimensional profiles were created that are placed perpendicular to the 2D geo-electric strike of the surrounding data. These profiles show the electrical conductivity of the region, from which it can be seen that there are similarities and large connecting features that affect the entire region. There are areas of expected high

resistivity which correspond to the regional geological features; however there are also areas of lower resistivity that have the same lithological units. This indicates that there has been a phase of alteration in the Earth to cause the change in resistivity.

The profiles are transected by a multitude of faults, of which the dominant NW-trend is overprinted by smaller NS-trending faults; these can be traced between the different profiles. The sub-surface features that have lowered resistivity appear to correspond to these fault systems, indicating involvement of the faults in the resistivity change. The most likely scenario is a change in resistivity due to fluid flow along these fault systems. The NW-trending fault is associated with enhanced conductivity from the upper mantle to upper crust, while the NS-trending faults are associated with increased resistivity in the mid crust. It is suggested that there are two phases of fluid flow to produce this scenario. The first fluid (sourced from the mantle) travels along the fault system depositing graphite due to its highly carbonic nature, as well as copper and gold. The second fluid phase would have probably originated from a meteoric source, possibly having involvement with crustal magmatism. This fluid would have travelled along the NS-trending faults, concentrating the copper and gold in the deposit and destroying the graphite in the mid crust. The two-phase model for fluid flow supports the models proposed by Oreskes and Einaudi (1990), Skirrow et al (2007), Bastrakov et al (2007), and Groves et al (2010), which include a hydrothermal fluid alteration system.

Acknowledgements

Thankyou to; TECK Resources Limited and BHP Billiton Limited for providing financial support for the study. I would like to thank Kate Selway for her outstanding support and contribution into the paper. Lisa Vella and Nick Hayward from TECK for their discussions contributing to the paper. Stephan Thiel for the codes that are used in producing phase tensor data and the processing of the data. Hamish Adam, Jonathan Ross and Kate Selway for data collection and processing. Goran Boren, Kathleen McClintock and Jarrad Hunt for data collection.

References

Bastrakov, E.N., Skirrow, R.G., and Didson, G.J., 2007, Fluid evolution and origins of iron oxide Cu-Au prospects in the Olympic Dam district, Gawler craton, south Australia: Economic Geology, v. 102, p. 1415-1440.

Belperio, A., Flint, R., and Freeman, H., 2007, Prominent Hill: A hematite-dominated, iron oxide copper-gold system: Economic Geology, v. 102, p. 1499-1510.

Blissett, A.H., Creaser, R.A., Daly, S., Flint, D.J., and Parker, A.J., 1993, Gawler Range Volcanics: The Precambrian: South Australia Geological Survey of South Australia, p. 107–131.

Budd, A.R., Wyborn, L.A.I., and Bastrakova, I.V., 2001, The metallogenic potential of Australian Proterozoic granites: Geoscience Australia, p. 152.

Caldwell, T.G., Bibby, H.M., and Brown, C., 2004, The magnetotelluric phase tensor: Geophysical Journal International, v. 158, p. 457-469.

Chave, A.D., and Thomson, D.J., 1989, SOME COMMENTS ON MAGNETOTELLURIC RESPONSE FUNCTION ESTIMATION: Journal of Geophysical Research-Solid Earth and Planets, v. 94, p. 14215-14225.

—, 2004, Bounded influence magnetotelluric response function estimation: Geophysical Journal International, v. 157, p. 988-1006.

Cooper, J.A., Mortimer, G.E., Rosier, C.M., and Uppill, R.K., 1985, GAWLER RANGE MAGMATISM FURTHER ISOTOPIC AGE DATA: Australian Journal of Earth Sciences, v. 32, p. 115-123.

Cowley, W.M., Conor, C.H.H., and Zang, W., 2003, New and revised Proterozoic stratigraphic units on northern Yorke Peninsula: MESA journal, v. 29, p. 46.

Creaser, R.A., 1995, NEODYMIUM ISOTOPIC CONSTRAINTS FOR THE ORIGIN OF MESOPROTEROZOIC FELSIC MAGMATISM, GAWLER-CRATON, SOUTH AUSTRALIA: Canadian Journal of Earth Sciences, v. 32, p. 460-471.

Daly, S.J., Fanning, C.M., and Fairclough, M.C., 1998, Tectonic evolution and exploration potential of the Gawler craton, South Australia: AGSO Journal of Australian Geology and Geophysics, v. 17, p. 145-168.

Direen, N.G., and Lyons, P., 2007, Regional crustal setting of iron oxide Cu-Au mineral systems of the Olympic Dam region, south Australia: Insights from potential-field modeling: Economic Geology, v. 102, p. 1397-1414.

Drummond, B., Lyons, P., Goleby, B., and Jones, L., 2006, Constraining models of the tectonic setting of the giant Olympic Dam iron oxide-copper-gold deposit,

South Australia, using deep seismic reflection data: Tectonophysics, v. 420, p. 91-103.

Fairclough, M., 2005, Geological and metallogenic setting of the Carrapateena Fe-O-Cu-Au prospect - a PACE success story: Mesa Hournal, v. 38, p. 4.

Fanning, C.M., Parker, A.J., Flint, R.B., Ludwig, K.R., and Blissett, A.H., 1988, REFINED PROTEROZOIC EVOLUTION OF THE GAWLER CRATON, SOUTH-AUSTRALIA, THROUGH U-PB ZIRCON GEOCHRONOLOGY: Precambrian Research, v. 40-1, p. 363-386.

Ferris, G.M., and Schwarz, M., 2004, Definition of the Tunkillia Suite, western Gawler Craton.: MESA Journal, v. 34, p. 32–41.

Flint, R.B., Rankin, L.R., and Fanning, C.M., 1990, Definition; the Palaeoproterozoic St. Peter Suite of the western Gawler craton: Geological Survey of South Australia, v. 114, p. 2-8.

Fraser, G.L., Skirrow, R.G., Schmidt-Mumm, A., and Holm, O., 2007, Mesoproterozoic Gold in the Central Gawler Craton, South Australia: Geology, Alteration, Fluids, and Timing: Economic Geology, v. 102, p. 1511-1539.

Glover, P.W.J., 1996, Graphite and electrical conductivity in the lower continental crust: A review: Physics and Chemistry of The Earth, v. 21, p. 279-287.

Groves, D.I., Bierlein, F.P., Meinert, L.D., and Hitzman, M.W., 2010, Iron Oxide Copper-Gold (IOCG) Deposits through Earth History: Implications for Origin, Lithospheric Setting, and Distinction from Other Epigenetic Iron Oxide Deposits: Economic Geology, v. 105, p. 641-654.

Hand, M., Reid, A., and Jagodzinski, L., 2007, Tectonic framework and evolution of the Gawler craton, southern Australia: Economic Geology, v. 102, p. 1377-1395.

Haynes, D.W., Cross, K.C., Bills, R.T., and Reed, M.H., 1995, Olympic Dam ore genesis; a fluid-mixing model: Economic Geology, v. 90, p. 281-307.

Heinson, G.S., Direen, N.G., and Gill, R.M., 2006, Magnetotelluric evidence for a deep-crustal mineralizing system beneath the Olympic Dam iron oxide copper-gold deposit, southern Australia: Geology, v. 34, p. 573-576.

Hermance, J.F., 1979, ELECTRICAL-CONDUCTIVITY OF MATERIALS CONTAINING PARTIAL MELT - SIMPLE-MODEL FROM ARCHIES LAW: Geophysical Research Letters, v. 6, p. 613-616.

Hitzman, M.W., Oreskes, N., and Einaudi, M.T., 1992, GEOLOGICAL CHARACTERISTICS AND TECTONIC SETTING OF PROTEROZOIC IRON-OXIDE (CU-U-AU-REE) DEPOSITS: Precambrian Research, v. 58, p. 241-287.

Jagodzinski, E.A., 2005, Compilation of SHRIMP U-Pb geochronological data, Olympic Domain, Gawler craton, South Australia.: Geoscience Australia, p. 211.

Jones, A.G., Ledo, J., Ferguson, I.J., Farquharson, C., Garcia, X., Grant, N., McNeice, G., Roberts, B., Spratt, J., Wennberg, G., Wolynec, L., and Wu, X.H., 2005, The electrical resistivity structure of Archean to Tertiary lithosphere along 3200 km of SNORCLE profiles, northwestern Canada: Canadian Journal of Earth Sciences, v. 42, p. 1257-1275.

Menezes, P.T.L., and Travassos, J.M., 2010, Magnetotellurics as a modeling tool in the extensive magmatic context of Parana Basin, Brazil: The Leading Edge, v. 29, p. 832-840.

Mortimer, G.E., Cooper, J.A., and Oliver, R.L., 1988, The geochemical evolution of Proterozoic granitoids near Port Lincoln in the Gawler orogenic domain of South Australia: Precambrian Research, v. 40-41, p. 387-406.

Nover, G., 2005, Electrical Properties of Crustal and Mantle Rocks – A Review of Laboratory Measurements and their Explanation: Surveys in Geophysics, v. 26, p. 593-651.

Oliver, R.L., and Fanning, C.M., 1997, Australia and Antarctica; precise correlation of Palaeoproterozoic terrains: The Antarctic region; Geological evolution and processes: Proceedings of the VII International Symposium on Antarctic Earth Sciences, Siena, Italy, Terra Antarctica Publication, p. 163-172.

Oreskes, N., and Einaudi, M.T., 1990, ORIGIN OF RARE-EARTH ELEMENT-ENRICHED HEMATITE BRECCIAS AT THE OLYMPIC-DAM CU-U-AU-AG DEPOSIT, ROXBY DOWNS, SOUTH AUSTRALIA: Economic Geology and the Bulletin of the Society of Economic Geologists, v. 85, p. 1-28.

—, 1992, ORIGIN OF HYDROTHERMAL FLUIDS AT OLYMPIC DAM - PRELIMINARY-RESULTS FROM FLUID INCLUSIONS AND STABLE ISOTOPES: Economic Geology and the Bulletin of the Society of Economic Geologists, v. 87, p. 64-90.

Parkinson, W.D., 1962, The Influence of Continents and Oceans on Geomagnetic Variations: Geophysical Journal of the Royal Astronomical Society, v. 6, p. 441-449.

Payne, J.L., Barovich, K.A., and Hand, M., 2006, Provenance of metasedimentary rocks in the northern Gawler Craton, Australia: Implications for palaeoproterozoic reconstructions: Precambrian Research, v. 148, p. 275-291.

Payne, J.L., Ferris, G., Barovich, K.M., and Hand, M., 2010, Pitfalls of classifying ancient magmatic suites with tectonic discrimination diagrams: An example from the Paleoproterozoic Tunkillia Suite, southern Australia: Precambrian Research, v. 177, p. 227-240.

Priess, W.V., 1987, The Adelaide Geosyncline — late Proterozoic stratigraphy, palaeontology and tectonics.: Geol. Surv. South Aust., v. 53, p. 438.

Rankin, L.R., Flint, R.B., and Fanning, C.M., 1990, Palaeoproterozoic Nuyts Volcanics of the western Gawler craton, South Australia.: Department of Primary Industries and Resources, p. 17.

Reeve, J.S., Cross, K.C., Smith, R., and Oreskes, N., 1990, Olympic Dam copper-uranium-gold-silver deposit.: Geology of the mineral deposits of Australia and Papua New Guinea, v. Monograph 14, p. 26.

Roberts, D.E., and Hudson, G.R.T., 1983, THE OLYMPIC DAM COPPER-URANIUM-GOLD DEPOSIT, ROXBY DOWNS, SOUTH-AUSTRALIA: Economic Geology, v. 78, p. 799-822.

Rodi, W., and Mackie, R.L., 2001, Nonlinear conjugate gradients algorithm for 2-D magnetotelluric inversion: Geophysics, v. 66, p. 174-187.

Selway, K., Hand, M., Heinson, G.S., and Payne, J.L., 2009a, Magnetotelluric constraints on subduction polarity: Reversing reconstruction models for Proterozoic Australia: Geology, v. 37, p. 799-802.

Selway, K., Heinson, G., and Hand, M., 2006, Electrical evidence of continental accretion: Steeply-dipping crustal-scale conductivity contrast: Geophysical Research Letters, v. 33.

Selway, K., Sheppard, S., Thorne, A.M., Johnson, S.P., and Groenewald, P.B., 2009b, Identifying the lithospheric structure of a Precambrian orogen using magnetotellurics: The Capricorn Orogen, Western Australia: Precambrian Research, v. 168, p. 185-196.

Simpson, F., and Bahr, K., 2005, Practical Magnetotellurics.

Skirrow, R.G., Bastrakov, E.N., Baroncii, K., Fraser, G.L., Creaser, R.A., Fanning, C.M., Raymond, O.L., and Davidson, G.J., 2007, Timing of iron oxide Cu-Au-(U) hydrothermal activity and Nd isotope constraints on metal sources in the Gawler craton, south Australia: Economic Geology, v. 102, p. 1441-1470.

Skirrow, R.G., Bastrakov, E.N., and Barovich, K., 2006, Metals and fluids in IOCG systems of the Gawler Craton: Constraints from Nd, O, H and S isotopes: Geochimica Et Cosmochimica Acta, v. 70, p. A595-A595.

Skirrow, R.G., Bastrakov, E.N., Davidson, G.J., Raymond, O.L., and Heithersay, P., 2002, The geological framework, distribution and controls of Fe-oxide and related alteration, and Cu-Au mineralisation in the Gawler craton, South Australia. Part II: Alteration and mineralisation: Hydrothermal iron oxide copper-gold and related deposits: A global perspective, 2: Adelaide, Porter GeoConsultancy Publishing, p. 33-47.

Stewart, K.P., and Foden, J., 2003, Mesoproterozoic granites of South Australia: South Australia Department of Primary Industries and Resources, v. 2003.

Swain, G., Barovich, K., Hand, M., and Ferris, G., 2005, Proterozoic magmaticarcs and oroclines: St Peter Suite, Gawler craton, South Australia.: Supercontinents and Earth Evolution Symposium 2005, Geological Society of Australia,, p. 42.

Swift, C.M., 1971, Theoretical Magnetotelluric and Turam response from twodimensional inhomogeneities,: Geophys., v. 36, p. 38-52.

Turner, S., Foden, J., Sandiford, M., and Bruce, D., 1993, SM-ND ISOTOPIC EVIDENCE FOR THE PROVENANCE OF SEDIMENTS FROM THE ADELAIDE FOLD BELT AND SOUTHEASTERN AUSTRALIA WITH IMPLICATIONS FOR EPISODIC CRUSTAL ADDITION: Geochimica Et Cosmochimica Acta, v. 57, p. 1837-1856.

Vella, L., 1997, Interpretation and modelling, based on petrophysical measurements, of the Wirrda well potential field anomaly, South Australia: Exploration Geophysics, v. 28, p. 299-306.

Vella, L., and Emerson, D., 2009, Carrapateena: physical properties of a new iron-oxide copper-gold deposit: ASEG Extended Abstracts, v. 2009, p. -.

Vozoff, K., 1972, The magnetotelluric method in the exploration of sedimentary basins: Geophys., v. 37, p. 98-141.

Wannamaker, P.E., and Doerner, W.M., 2002, Crustal structure of the Ruby Mountains and southern Carlin Trend region, Nevada, from magnetotelluric data: Ore Geology Reviews, v. 21, p. 185-210.

Wannamaker, P.E., Doerner, W.M., Stodt, J.A., and Johnston, J.M., 1997, Subdued state of tectonism of the Great Basin interior relative to its eastern margin based on deep resistivity structure: Earth and Planetary Science Letters, v. 150, p. 41-53.

Williams, P.J., Barton, M.D., Fontboté, L., de Haller, A., Johnson, D.A., Mark, G., Marschik, R., and Oliver, N.H.S., 2005, Iron-oxide-copper-gold deposits: Gology, space-time distribution, and possible modes of origin: Economic Geology 100th Anniversary Volume, p. 35.

Figure Captions

Figure 1: Greyscale Total Magnetic Intensity map of the study area showing station locations, faults and the profiles used for the 2D modelling process. Inset map showing the location of the stations relative to South Australia and the Gawler Craton.

Figure 2: Apparent resistivity (in ohm metres) and phase (in degrees) against period (seconds) for 4 stations that represent the data for the region, one from each year of collection. Circles (red) represent TE mode data and the squares (blue) represent TM mode data. Each station is a representation of good

quality data, shown by smooth apparent resistivity and phase curves with small error bars. St77 from 2009 is a good example of poor data for short and long periods, shown by large error bars.

Figure 3: Induction arrows at periods 100s, 500s, 1000s and 2000s for all MT stations. Induction arrows are using the Parkinson convention and therefore are pointing towards the regions of enhanced conductivity (Parkinson, 1962). Increasing periods correspond to increasing skin depth from the MT station.

Figure 4: Modified from Caldwell et al (2004), this is the graphical representation of the MT phase tensor. The axes of the ellipse are proportional to the principal values of the phase tensor. The relationship between alpha and the skew defines the tensor on the user's reference grid. The orientation of the maximum phase axis of the ellipse represents the geo-electric strike.

Figure 5: Phase tensors ellipse for all MT stations at a period of 128 seconds on a TMI background. The geo-electric strike can be seen to change throughout the region.

Figure 6: Root mean squared (rms) error is plotted against tau for 2D models that have been run for 100 iterations. The tau parameter represents the ratio between the smoothness and the roughness of the model's data fit. It can be seen that a tau value between 1 and 3 marks a change in gradient in the curve, choosing a value lower than this increase the structure in the model without providing an increase in data fit.

Figure 7: The 2D model formed from a smooth inversion (Rodi and Mackie, 2001) that represents the 20 degree profile. The model was calculated with a maximum data error in apparent resistivity of 10% and the final root mean square (rms) value was 3.4225.

Figure 8: The 2D model formed from a smooth inversion (Rodi and Mackie, 2001) that represents the 10 degree profile. The model was calculated with a maximum data error in apparent resistivity of 10% and the final root mean square value was 1.7949.

Figure 9: The 2D model formed from a smooth inversion (Rodi and Mackie, 2001) that represents the 40 degree profile. The model was calculated with a maximum data error in apparent resistivity of 10% and the final root mean square value was 1.8912.

Figure 10: Depth slices of the two 3D forward models produced. The sedimentary basins model's major conductive regions are based on the depth to basement, for an area surrounding the stations to a distance of 400km. The conductive region was set to 10 ohm metres, while the resistive region was set to 4000 ohm metres.
The curved conductor model represents an extrapolation of the 2D models highlighting the conductive and resistive zones. The resistive region is set to 4000 ohm metres, while the conductive region is set to 100 ohm metres.

Figure 11: Induction arrows for the 3D forward models, at periods of 100s and 500s, for all MT stations. Induction arrows are using the Parkinson convention and therefore are pointing towards the regions of enhanced conductivity (Parkinson, 1962). Increasing periods correspond to increasing penetration depth from the MT station.

Appendix

See attached PDF

Figures

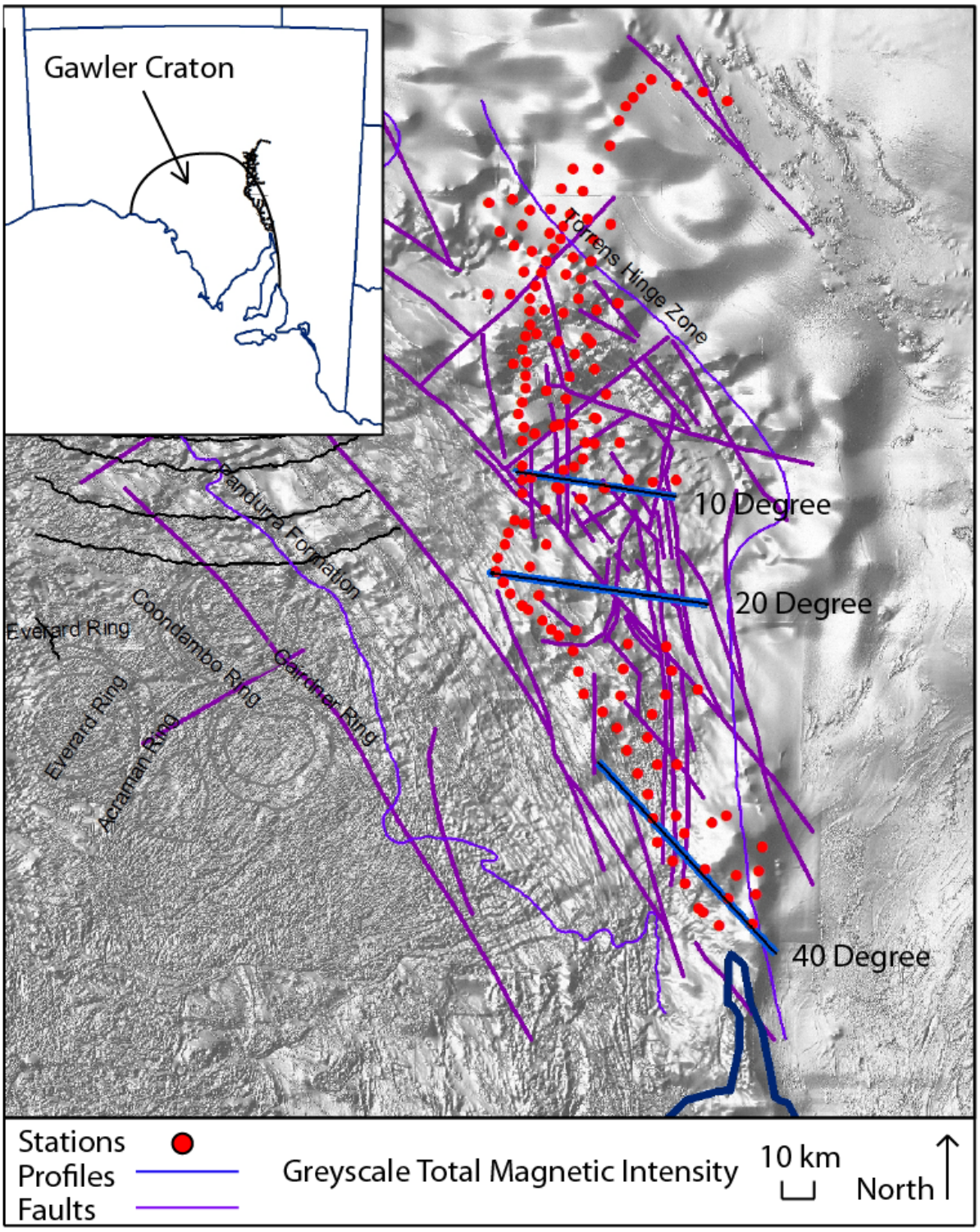

Figure 1

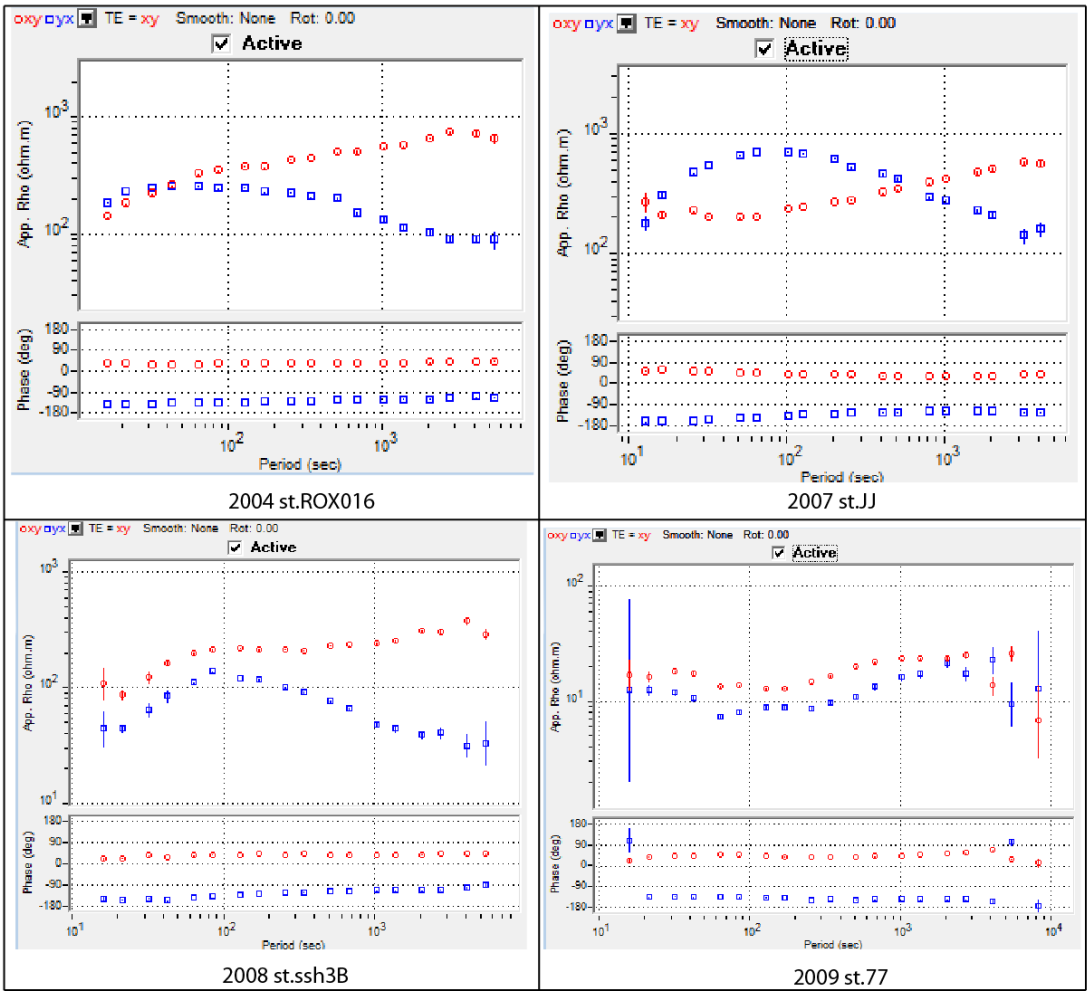
oxy oyx TE = xy Smooth: None Rot: 0.00
Active
App. Rho (ohm.m)
Phase (deg)
Period (sec)
2004 st.ROX016
2007 st.JJ
2008 st.ssh3B
2009 st.77

Figure 2

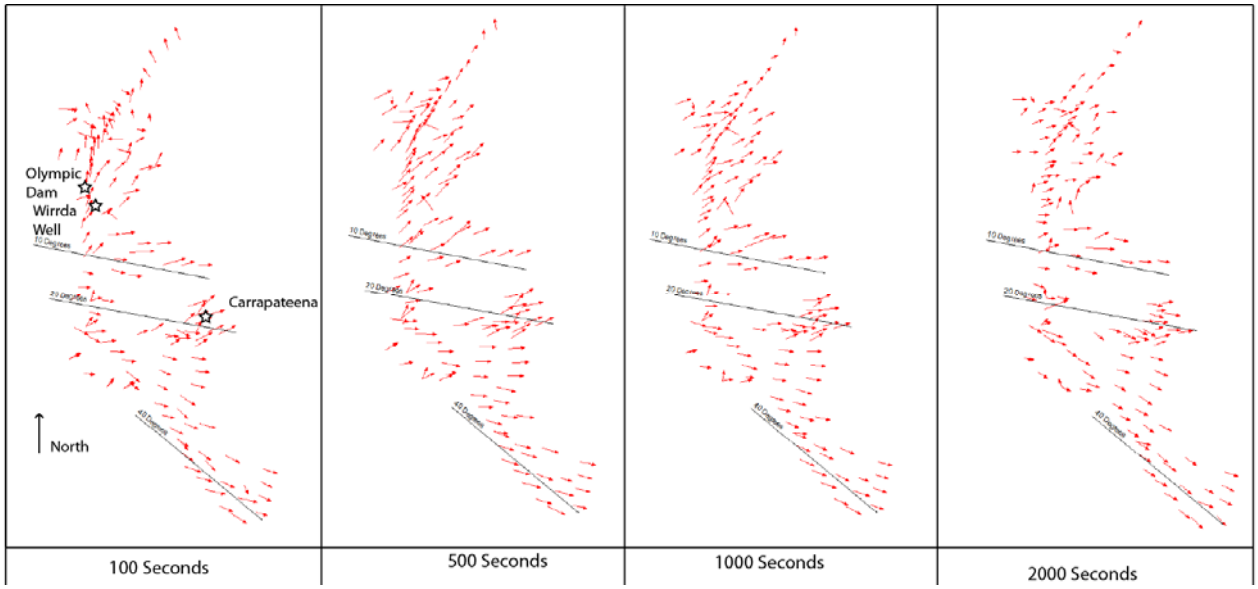
Olympic Dam
Wirrda Well
Carrapateena
North
100 Seconds
500 Seconds
1000 Seconds
2000 Seconds

Figure 3

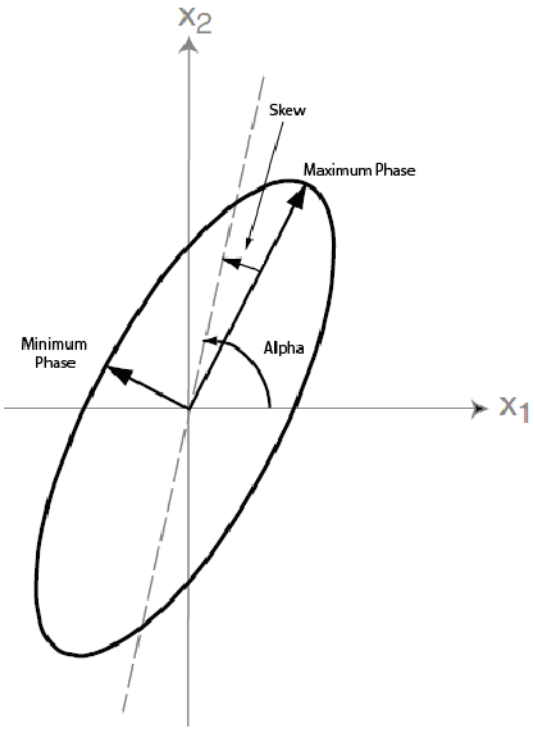

Figure 4

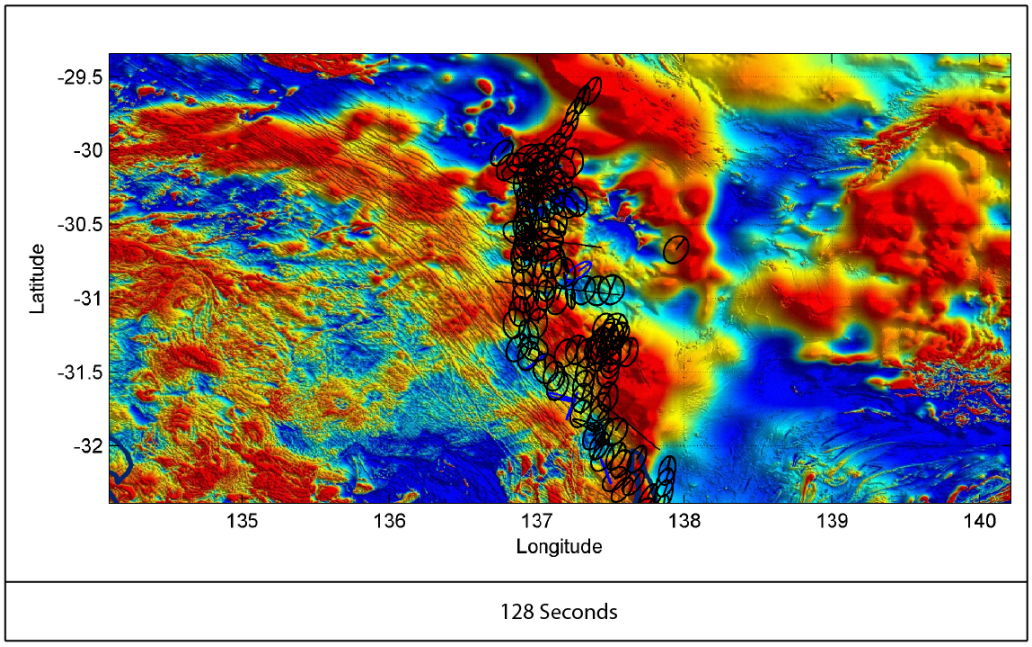
-29.5
-30
-30.5
-31
-31.5
-32
Latitude
135
136
137
138
139
140
Longitude
128 Seconds

Figure 5

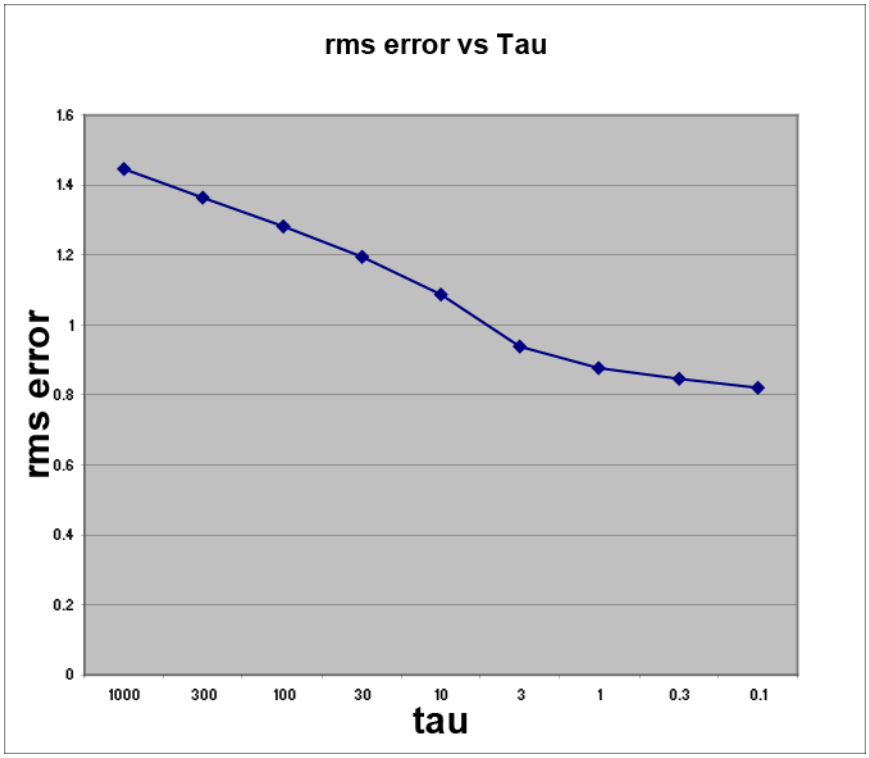
rms error vs Tau
rms error
1.6
1.4
1.2
1
0.8
0.6
0.4
0.2
0
1000
300
100
30
10
3
1
0.3
0.1
tau

Figure 6

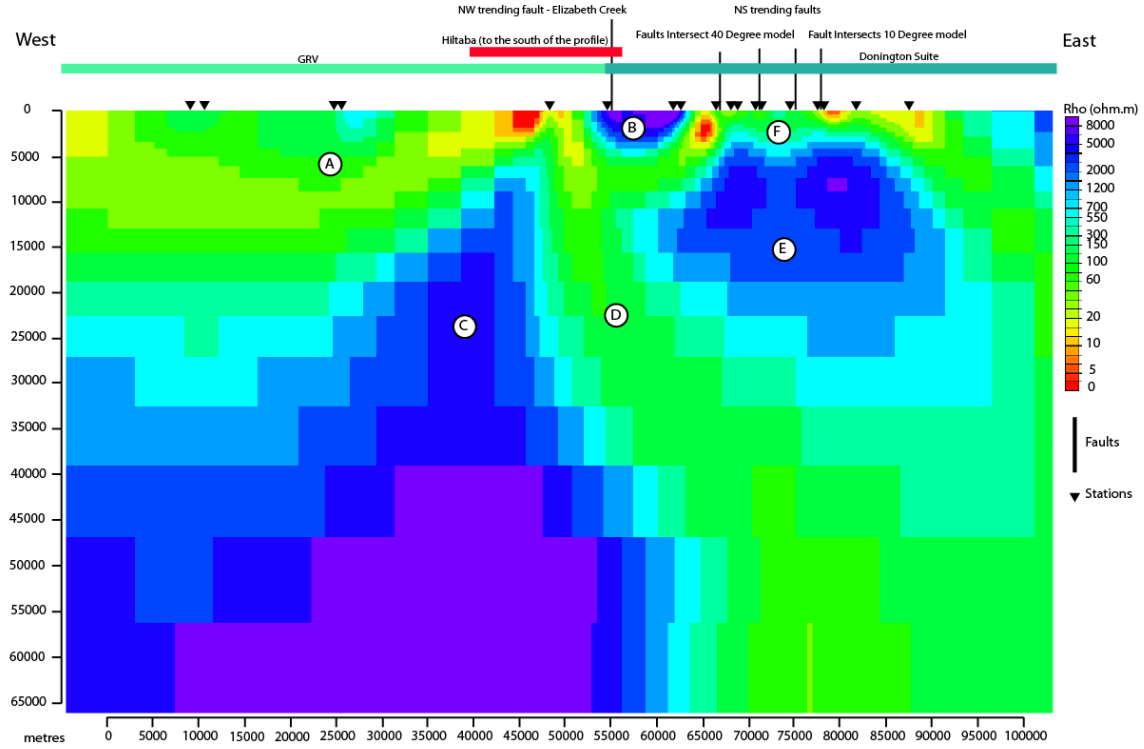
NW trending fault - Elizabeth Creek
NS trending faults
Hiltaba (to the south of the profile)
Faults Intersect 40 Degree model
Fault Intersects 10 Degree model
West
East
GRV
Donington Suite
Rho (ohm.m)
8000
5000
2000
1200
700
550
300
150
100
60
20
10
5
0
Faults
Stations
A
B
C
D
E
F
0
5000
10000
15000
20000
25000
30000
35000
40000
45000
50000
55000
60000
65000
metres
0
5000
10000
15000
20000
25000
30000
35000
40000
45000
50000
55000
60000
65000
70000
75000
80000
85000
90000
95000
100000

Figure 7

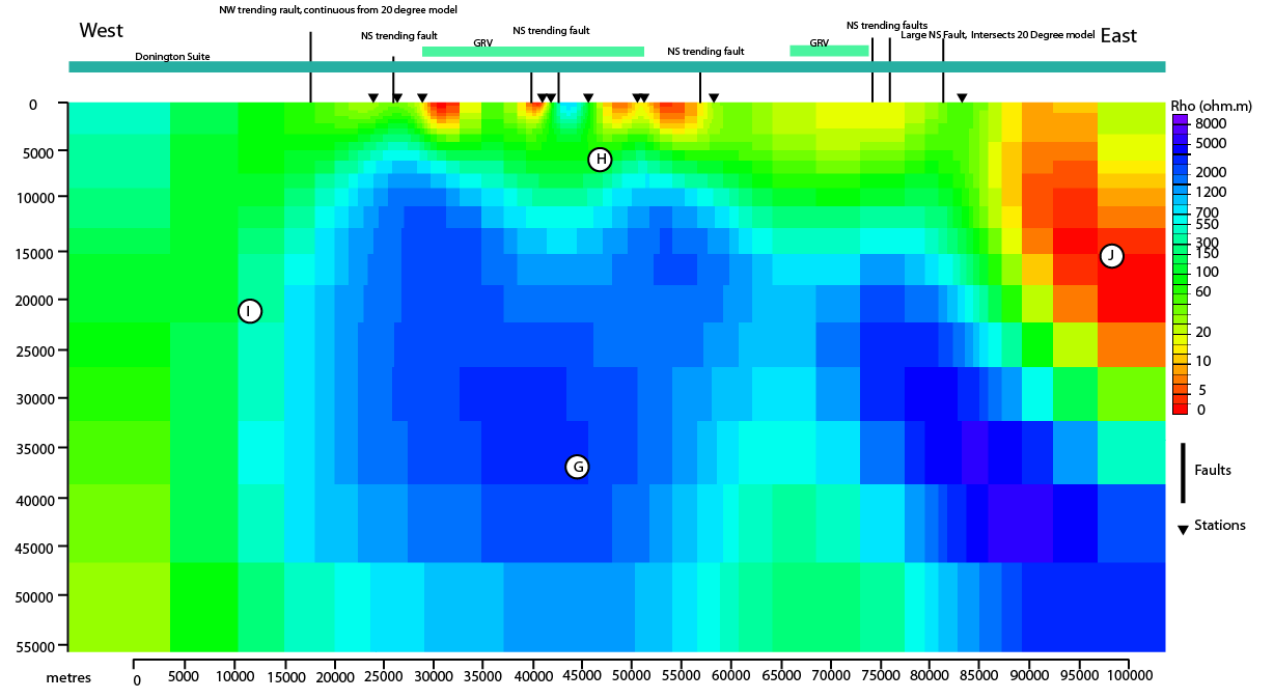
West
East
NW trending rault, continuous from 20 degree model
NS trending fault
GRV
NS trending fault
NS trending fault
GRV
NS trending faults
Large NS Fault, Intersects 20 Degree model
Donington Suite
H
I
J
G
Rho (ohm.m)
8000
5000
2000
1200
700
550
300
150
100
60
20
10
5
0
Faults
Stations
metres
0
5000
10000
15000
20000
25000
30000
35000
40000
45000
50000
55000
60000
65000
70000
75000
80000
85000
90000
95000
100000

Figure 8

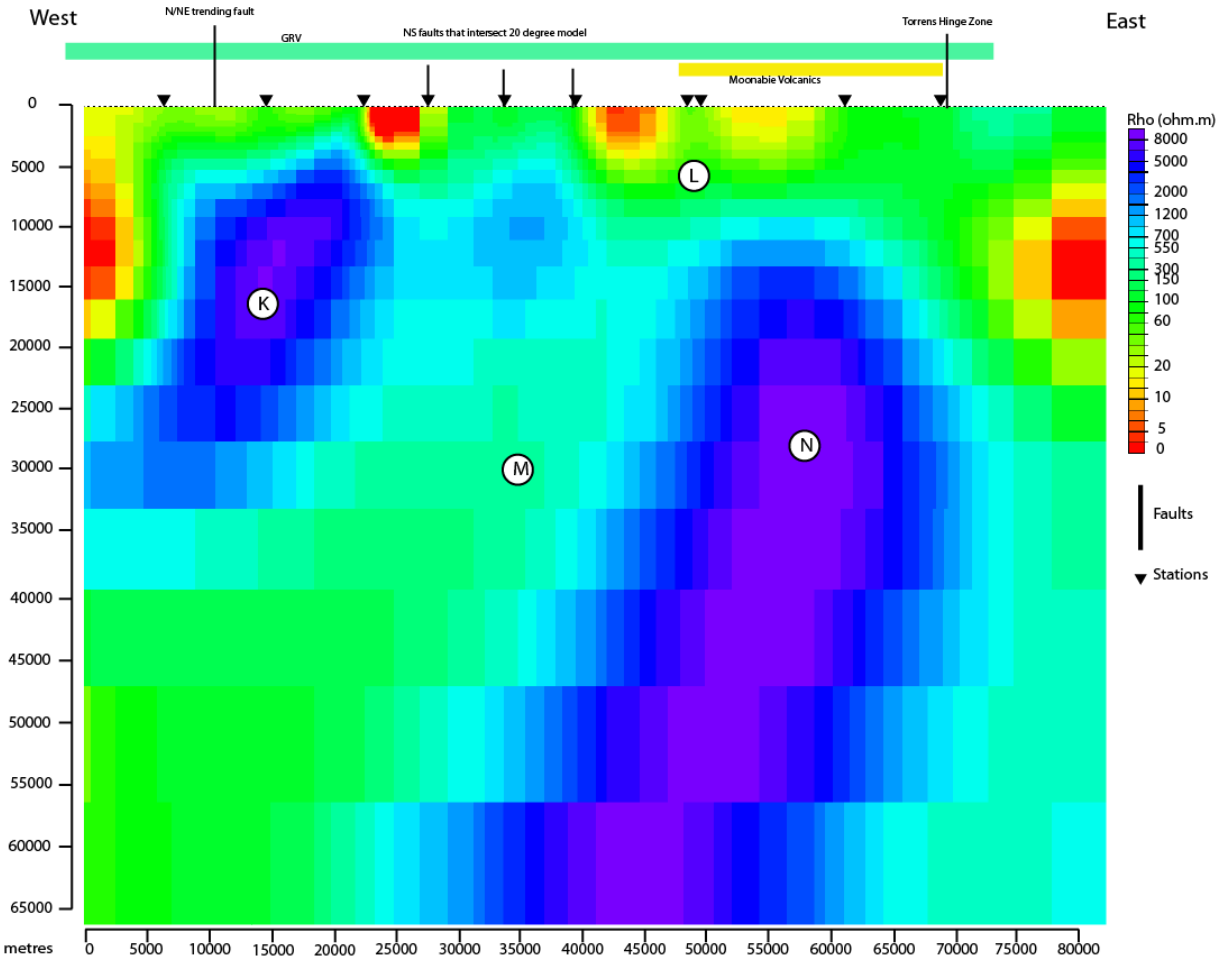
West
East
N/NE trending fault
GRV
NS faults that intersect 20 degree model
Torrens Hinge Zone
Moonabie Volcanics
K
L
M
N
Rho (ohm.m)
8000
5000
2000
1200
700
550
300
150
100
60
20
10
5
0
Faults
Stations
0
5000
10000
15000
20000
25000
30000
35000
40000
45000
50000
55000
60000
65000
metres
0
5000
10000
15000
20000
25000
30000
35000
40000
45000
50000
55000
60000
65000
70000
75000
80000

Figure 9

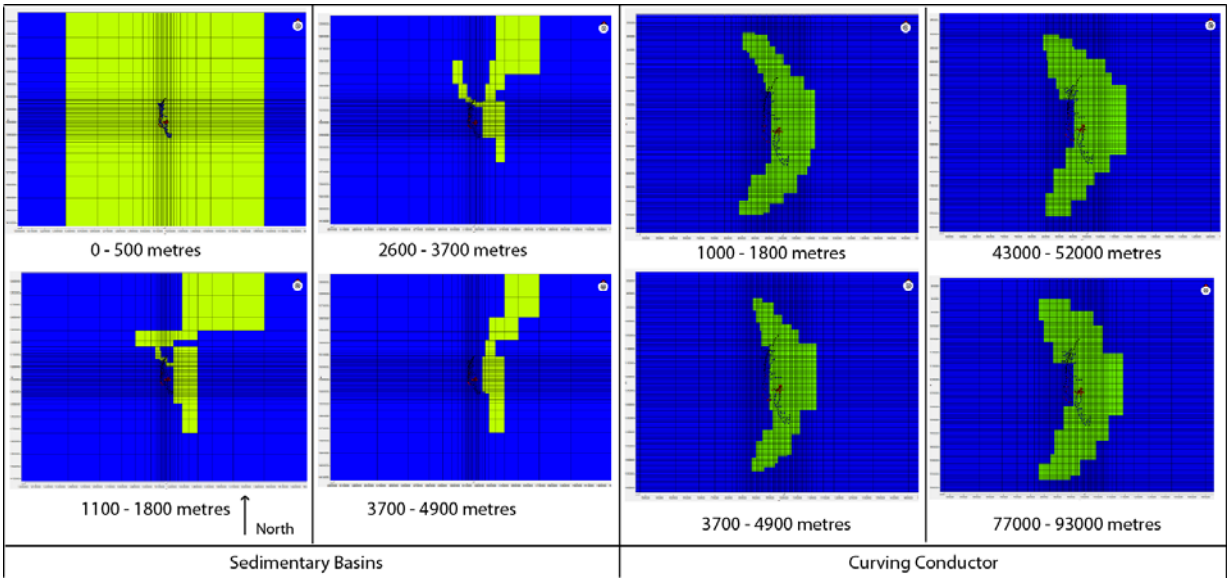
0 - 500 metres
2600 - 3700 metres
1000 - 1800 metres
43000 - 52000 metres
1100 - 1800 metres
North
3700 - 4900 metres
3700 - 4900 metres
77000 - 93000 metres
Sedimentary Basins
Curving Conductor

Figure 10

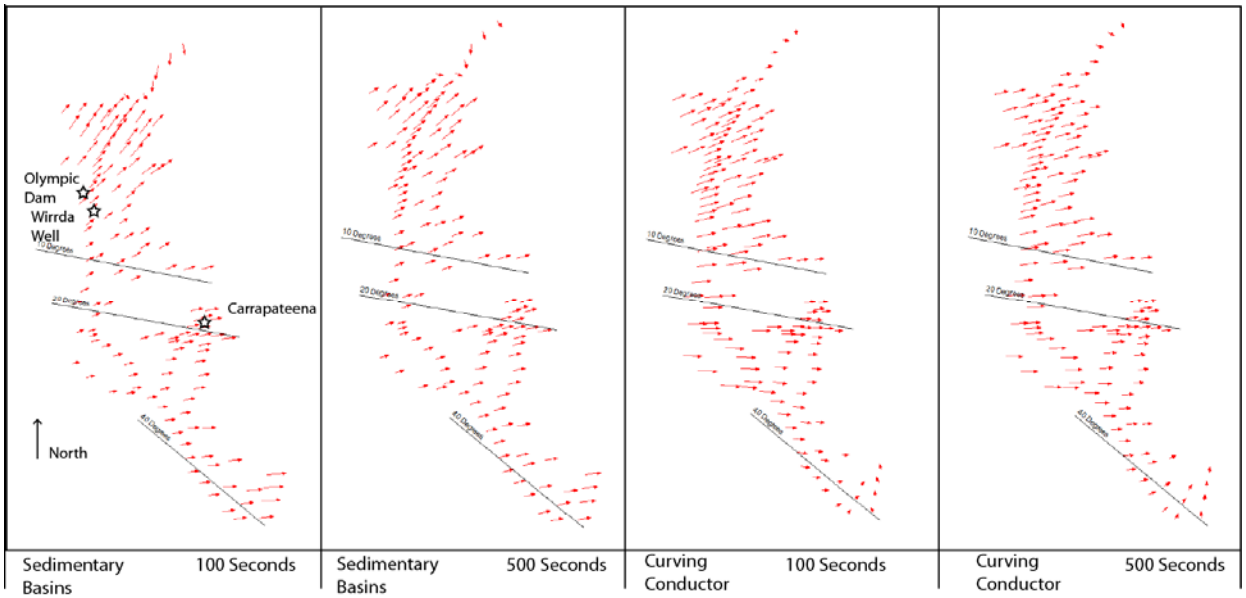
Olympic Dam
Wirrda Well
Carrapateena
North
Sedimentary Basins
100 Seconds
Sedimentary Basins
500 Seconds
Curving Conductor
100 Seconds
Curving Conductor
500 Seconds

Figure 11

Station name	Eastings	Northings	Elevation	Zxy impeda	Zyx impeda	R12 phase	R21 phase
2009							
1	755566	6407713	3.9	Positive	Negative	On Phase	On Phase
2	748018	6414079	4.2				
3	742836	6423541	7.1	Positive	Negative	On Phase	On Phase
4	738310	6431637	6.0	Positive	Negative	On Phase	On Phase
5	732555	6438655	62.0	Positive	Negative	On Phase	On Phase
6	730771	6447923	77.0	Positive	Negative	On Phase	On Phase
7	729152	6456744	103.9				
8	725064	6464397	98.6	Positive	Negative	On Phase	On Phase
9	721280	6473210	81.9	Positive	Negative	On Phase	On Phase
10	717584	6481500	99.0	Positive	Negative	On Phase	On Phase
11	712175	6487733	74.0	Positive	Negative	On Phase	Off Phase
12	705165	6494314	93.0	Random	Random	Off Phase	Off Phase
13	703247	6502818	156.0	Positive	Negative	On Phase	On Phase
14	701178	6510263	174.0	Positive	Negative	On Phase	On Phase
15	695581	6516062	106.0	Positive	Negative	On Phase	On Phase
16	689805	6521612	74.0	Random	Random	Off Phase	Off Phase
17	684432	6525705	122.0	Positive	Negative	On Phase	On Phase
18	677543	6531889	189.0	Positive	Negative	On Phase	On Phase
19	771798	6437225	53.0	Positive	Negative	On Phase	On Phase
20	762019	6426412	25.2	Positive	Negative	On Phase	On Phase
21	770315	6428212	123.0	Positive	Negative	On Phase	On Phase
22	769290	6419476	54.0	Positive	Negative	On Phase	On Phase
23	758881	6417862	20.5	Random	Random	Off Phase	Off Phase
24	749662	6412626	40.4	Positive	Negative	On Phase	On Phase
25	750168	6428794	28.0	Positive	Negative	On Phase	On Phase
26	767969	6408484	39.0	Positive	Negative	Off Phase	Off Phase
27	758155	6448776	45.2				
28	752845	6446054	78.1	Positive	Negative	On Phase	On Phase
29	739416	6448811	64.2	Positive	Negative	On Phase	On Phase
30	742488	6442159	46.4	Positive	Negative	On Phase	On Phase
31	739830	6467934	54.2	Positive	Negative	On Phase	On Phase
32	732434	6467833	32.8	Positive	Negative	On Phase	On Phase
33	728898	6456835	111.1	Random	Random	Off Phase	Off Phase
34	747532	6496036	67.2	Positive	Negative	On Phase	On Phase
35	735804	6511869	120.7	Positive	Negative	On Phase	On Phase
36	737784	6502853	96.7	Positive	Negative	On Phase	On Phase
37	735429	6494101	91.9	Positive	Negative	On Phase	On Phase
38	730395	6486534		Positive	Negative	On Phase	On Phase
39	728770	6477902	77.7	Positive	Negative	On Phase	On Phase
40	721522	6512915	70.5	Positive	Negative	On Phase	On Phase
41	719819	6503530	75.1	Positive	Negative	On Phase	On Phase
42	718846	6493719	77.2	Positive	Negative	On Phase	On Phase
43	729031	6456859	115.5	Positive	Negative	On Phase	On Phase
44	688447	6530948	196.8	Random	Random	Off Phase	Off Phase
45	691168	6550047	150.6	Positive	Negative	Off Phase	Off Phase
46	684918	6541936	148.8	Random	Random	Off Phase	Off Phase
47	712808	6571254	131.7	Random	Random	Off Phase	Off Phase
48	704430	6567120	140.7	Positive	Negative	Off Phase	Off Phase
49	739401	6574165	63.6	Positive	Negative	Off Phase	Off Phase
50	730694	6573556	84.9	Positive	Negative	Off Phase	Off Phase

51	721449	6574202	152.6	Positive	Negative	Off Phase	Off Phase
52	696217	6570831	122.3	Positive	Negative	Off Phase	Off Phase
53	690700	6563350	138.9	Positive	Negative	Off Phase	Off Phase
54	718493	6588343	132	Random	Random	Off Phase	Off Phase
55	709123	6587998	123.4	Random	Random	Off Phase	Off Phase
56	697461	6577764	113.7	Positive	Negative	On Phase	Off Phase
57	704694	6582221	103.5	Random	Random	Off Phase	Off Phase
58	694079	6594202	100	Random	Random	Off Phase	On Phase
59	709141	6597555	65.3	Random	Random	Off Phase	Off Phase
60	700982	6594824	98.7	Positive	Negative	On Phase	On Phase
61	698554	6604581	101.9	Positive	Negative	On Phase	On Phase
62	690893	6607757	105	Positive	Negative	On Phase	On Phase
63	699665	6613065	120	Positive	Negative	On Phase	On Phase
64	701603	6621407	118	Positive	Negative	On Phase	On Phase
65	705955	6627275	126	Positive	Negative	On Phase	On Phase
66	694908	6625692	114	Positive	Negative	On Phase	On Phase
67	678751	6617627	94	Positive	Negative	On Phase	On Phase
68	687433	6629173	114	Positive	Negative	On Phase	On Phase
69	690424	6637664	106	Random	Random	On Phase	On Phase
70	697570	6636656	78	Positive	Negative	On Phase	On Phase
71	703239	6642071	68	Positive	Negative	On Phase	On Phase
72	701250	6657466	110	Positive	Negative	On Phase	On Phase
73	707767	6656065	40	Positive	Negative	On Phase	On Phase
74	698501	6651010	60	Positive	Negative	On Phase	On Phase
75	709893	6637680	70	Positive	Negative	On Phase	On Phase
76	717709	6640578	61	Positive	Negative	On Phase	On Phase
77	708648	6664274	49	Positive	Negative	On Phase	On Phase
78	704234	6649394	49	Positive	Negative	On Phase	On Phase
79	669685	6677753	128	Positive	Negative	On Phase	On Phase
80	678292	6679258	123	Positive	Negative	On Phase	On Phase
81	685204	6675190	114	Random	Negative	Off Phase	On Phase
82	673595	6667294	130	Random	Negative	Off Phase	On Phase
83	682042	6669429	93	Positive	Negative	On Phase	On Phase
84	679069	6661929	74	Positive	Negative	On Phase	On Phase
85	692692	6675588	112	Positive	Negative	On Phase	On Phase
86	692243	6666606	113	Positive	Negative	On Phase	On Phase
87	685801	6659782	78	Positive	Negative	On Phase	On Phase
88	682770	6651975	76	Positive	Negative	On Phase	On Phase
89	715012	6669720	89	Positive	Negative	On Phase	On Phase
90	706533	6672018	92	Positive	Negative	On Phase	On Phase
91	696727	6683078	96	Positive	Negative	On Phase	On Phase
92	701144	6690436		Positive	Negative	On Phase	On Phase
93	669159	6643839	101	Positive	Negative	On Phase	On Phase
94	677787	6643710	118	Positive	Negative	On Phase	On Phase
2007							
CC	741118.026	6545688.959	51	Positive	Negative	On Phase	On Phase
DD	739113.113	6541389.686	0	Positive	Negative	On Phase	On Phase
EE	735643.999	6539002.811	0	Positive	Negative	On Phase	On Phase
FF	742777.595	6539549.183	98	Positive	Negative	On Phase	On Phase
GG	733888.962	6545790.344	103	Positive	Negative	On Phase	On Phase

HH	737729.776	6534086.981	160	Positive	Negative	On Phase	On Phase
II	738279.545	6529174.787	168	Positive	Negative	On Phase	On Phase
KK	732624.916	6529394.383	136	Positive	Negative	On Phase	On Phase
LL	728352.867	6529950.619	127	Positive	Negative	On Phase	On Phase
MM	722841.322	6526957.296	93	Positive	Negative	On Phase	On Phase
NN	716078.306	6529748.888	80	Positive	Negative	On Phase	On Phase
OO	708969.519	6527305.183	69	Positive	Negative	On Phase	On Phase
PP	743853.457	6528892.371	210	Positive	Negative	On Phase	On Phase
QQ	749364.193	6527067.534	84	Positive	Negative	On Phase	On Phase
RR	723197.606	6525070.138	109	Positive	Negative	On Phase	On Phase
SS	725471.087	6520183.682	85	Positive	Negative	On Phase	On Phase
TT	729449.923	6524503.392	195	Positive	Negative	On Phase	On Phase
UU	738169.882	6523198.961	177	Positive	Negative	On Phase	On Phase
VV	737489.875	6518869.36	120	Positive	Negative	On Phase	On Phase
2004							
ROX1							
1	675729.023	6550038.312	118	Positive	Negative	On Phase	On Phase
3	679402.422	6559081.547	142	Positive	Negative	On Phase	On Phase
5	681879.442	6569348.704	147	Positive	Negative	On Phase	On Phase
7	682060.482	6579467.013	121	Positive	Negative	On Phase	On Phase
9	681900.379	6589092.02	101	Positive	Negative	On Phase	On Phase
11	680807.274	6598988.271	117	Positive	Negative	On Phase	On Phase
12	681951.755	6603407.261	83	Positive	Negative	On Phase	On Phase
13	683248.781	6608605.892	112	Positive	Negative	On Phase	On Phase
14	683454.869	6613361.013	98	Positive	Negative	On Phase	On Phase
15	683847.192	6618251.542	110	Positive	Negative	On Phase	On Phase
16	681901.899	6622882.821	91	Positive	Negative	On Phase	On Phase
17	683240.434	6627920.601	107	Positive	Negative	On Phase	On Phase
18	685061.738	6632404.896	97	Positive	Negative	On Phase	On Phase
19	685047.004	6637342.29	92	Positive	Negative	On Phase	On Phase
20	685128.275	6641966.947	104	Positive	Negative	On Phase	On Phase
21	687118.269	6646937.858	89	Positive	Negative	On Phase	On Phase
22	689244.477	6651804.5	91	Positive	Negative	On Phase	On Phase
23	691075.041	6656032.27	94	Positive	Negative	On Phase	On Phase
24	693856.415	6660686.567	109	Positive	Negative	On Phase	On Phase
25	696261.387	6664527.734	93	Positive	Negative	On Phase	On Phase
26	697432.112	6669345.494	104	Positive	Negative	On Phase	On Phase
27	700194.031	6673647.747	100	Positive	Negative	On Phase	On Phase
29	704838.46	6682362.375	92	Positive	Negative	On Phase	On Phase
31	710518.66	6690563.052	82	Positive	Negative	On Phase	On Phase
33	714901.415	6699171.531	75	Positive	Negative	On Phase	On Phase
35	717990.895	6708820.523	15	Positive	Negative	On Phase	On Phase
37	723630.603	6717398.754	3	Positive	Negative	On Phase	On Phase
39	730043.366	6723876.554	2	Positive	Negative	On Phase	On Phase
ROX2							
0	672959.162	6545063.508	114	Positive	Negative	On Phase	On Phase
2	677041.399	6554384.046	149				
6	682176.927	6574321.169	132	Positive	Negative	On Phase	On Phase
10	682826.146	6594112.192	132				

102	682826.146	6594112.192	132	Positive	Negative	On Phase	On Phase
36	720815.394	6714078.586	18	Positive	Random	On Phase	On Phase
38	726617.735	6720754.909	10				
40	739766.552	6721652.227	19	Positive	Negative	On Phase	On Phase
41	749745.979	6719222.429	38	Positive	Negative	On Phase	On Phase
42	758739.507	6716085.184	82				
E01	707885.897	6625788.049	139	Positive	Negative	On Phase	On Phase
E02	709055.524	6615769.369	114	Positive	Negative	On Phase	On Phase
E03	713562.343	6606454.688	85	Positive	Negative	On Phase	On Phase
E04	709806.489	6597289.872	73	Positive	Negative	On Phase	On Phase
E05	705609.385	6588243.491	130	Positive	Negative	On Phase	On Phase
E05_2	705609.385	6588243.491	130	Positive	Negative	On Phase	On Phase
E06	701592.459	6579109.279	114	Positive	Negative	On Phase	On Phase
E07	695005.151	6571435.34	129	Positive	Negative	On Phase	On Phase
E07_2E08	695005.151	6571435.34	129	Positive	Negative	On Phase	On Phase
E09	703860.317	6567304.407	139	Positive	Negative	On Phase	On Phase
E10	712670.651	6571050.286	138	Positive	Negative	On Phase	On Phase
E11	721801.02	6574154.137	0	Positive	Negative	On Phase	On Phase
E13	695498.217	6626030.924	103	Positive	Negative	On Phase	On Phase
E14	696228.974	6594857.711	91				
N01	672231.953	6540261.189	179	Positive	Negative	On Phase	On Phase
2008							
Orange Boxes							
1a_LP	701939	6517915		Positive	Negative	On Phase	On Phase
1B_LP	693215	6518234		Positive	Negative	On Phase	On Phase
1B_LP_2	693215	6518234		Random	Random	Off Phase	Off Phase
1D_LP	682091	6527248		Positive	Negative	On Phase	On Phase
1D_LP_2	682091	6527248		Positive	Negative	On Phase	On Phase
1e_LP_2	674997	6535960		Positive	Negative	On Phase	On Phase
1E_LP_1A	674997	6535960		Positive	Negative	On Phase	On Phase
1E_LP_1D	674997	6535960		Positive	Negative	On Phase	On Phase
3A_LP	685529	6575313		Positive	Negative	On Phase	On Phase
3a_lp_2	685529	6575313		Positive	Negative	On Phase	On Phase
3B_LP	683121	6557705		Positive	Negative	On Phase	On Phase
3B_LP_2	683121	6557705		Positive	Negative	On Phase	On Phase
3C_LP	686746	6591542		Random	Random	Off Phase	Off Phase
3C_LP_2	686746	6591542		Random	Random	Off Phase	On Phase

Station name	1D	2D	3D	3D	2d Strike angle
2009					
1	<30	30><2000	>2000		40
2					50
3	<30	30><2000	>2000		40
4	30><50	50><2000	10><30	>2000	40
5					
6	40><100	100><2000	10><40	>2000	40
7					30
8	50	20><1000	>1000		30
9					
10	30><90	90><1000	>1000		25
11					
12					
13	30><90	90><1000	>1000		25
14	40><100	100><1000	<40	>1000	25
15	60><150		<60	>150	
16					
17	<60	60><200	>2000		20
18		<900	>900		40
19		<1000	>1000		10
20		>100	<100		20
21		>10			20
22		>10			20
23					
24		>30	<30		40
25		40><400	<40	>400	40
26					
27					
28		30><100	<30	>100	25
29		2D?			25
30	20><50	50><200			30
31	20><100	100><300	>300		25
32	20><90	>90			25
33	30><100				
34					
35	40><100	>100			15
36	60><100	<60 >100			15
37	40><90	90><200	<20 >200		20
38	40><80	>80			25
39	40><100	>100	<40		25
40	60><90	>90			20
41	40><100	>100	<40		20
42	50><90	>90	<50		20
43	30><70	<400	<30	>400	35
44					
45	30><50	>50	<30		20
46					
47					
48	30><100	100><600	<30	>600	15
49	60><100	100><1000	<60	>1000	10
50	40><100	100><1000	<40	>1000	10

51		100><1000			20
52		all			20
53	10><100	100><1000	>1000		20
54					
55	60><90		<60	>90	
56	20><60	>60			10
57					
58					
59					
60	40><100		>100		
61	30><100		>100		
62	30><100	>100			
63	30><100	>100			
64	30><70	>70			
65	30><80		>80		
66			all		
67			all		
68			all		
69					
70			all		
71			all		
72			all		
73			all		
74			all		
75			all		
76			all		
77			all		
78			all		
79			all		
80			all		
81		30><2000			50
82			all		
83					
84					
85	20><80	>80			60
86			all		
87	<90		>90		
88	30><80	>80			
89	<1000	>1000			20
90	all				40
91		all			75
92		all			75
93		100><1000			20
94		all			5
2007					
CC	80><150	50><80, 150>	<50	2 areas of	0
DD	100><150	50><100, 150>	<50		-20
EE	80><100	40><80, >100	<40		20
FF		>60	<60		20
GG	50><70	>70	<50		25

HH		>50	<50		15
II		>40	<40		-15
KK		>40	<40		15
LL	50><100	<50>100	<20		20
MM	50><100	<50>100	<20		20
NN	50><100	<50>100	<20	Check	20
OO		>30	<30	Check/ sk	15
PP	60><70	30><60, >70	<30		15
QQ		>30	<30		20
RR	40><100	30><40, >100	<30		15
SS	90><110	30><90, >110	<30		0
TT	50><80	30><50, >80	<30		15
UU	40><80	>80	<40		20
VV	40><80	>80	<40		0
2004					
ROX1					
1		>100	<100		10
3		>200	<200		15
5		>200	<200		10
7		>500	<500		10
9		>200	<200		15
11		>300	<300		0
12		>1000	<1000		10
13		>500	<500		10
14		>1000	<1000		10
15		>200	<200		0
16		>1000	<1000		10
17		>1000	<1000		15
18		>1000	<1000		
19		>1000	<1000		
20			all		
21			all		
22			all		
23			all		
24			all		
25			all		
26			all		
27			all		
29			all		
31		all			25
33		all			20
35		<100, >500	100><500		20
37		<150, >1000	150><1000		20
39			all		
ROX2					
0		>100	<100		15
2					
6					
10		>100	<100		5

102					
36			all		
38			40><1000		
40		20><100, >100	100><1000		25
41	>1000	20><100	100><1000		35
42					
E01		>1000	<1000		0
E02		>200	<200		0
E03		>1000	<1000		10
E04		>200	<200		0
E05			all		
E05_2					
E06		>100	<100		0
E07		>100	<100		0
E07_2E08		>200	<200		15
E09		>200	<200		15
E10		>100	<100		10
E11			20><1000		
E13		>600	<600		15
E14					
N01					
2008					
Orange Boxes					
1a_LP	50><150	<150	<50	15	
1B_LP		10><80, 150><	>200	15	
1B_LP_2	50><100	<50,>100		80	
1D_LP		>80	<80	15	
1D_LP_2		>70	<70	15	
1e_LP_2			20><100		
1E_LP_1A	Check Imp	Crap			
1E_LP_1D		Crap			
3A_LP		All		80	
3a_lp_2			all		
3B_LP	<120	>120		15	
3B_LP_2	Crap				
3C_LP	Crap				
3C_LP_2	Crap				